Untangling the solar wind and magnetospheric drivers of the radiation belt electrons

Simon Wing[1], Jay R. Johnson[2], Drew L. Turner[1], Aleksandr Y. Ukhorskiy[1], and Alexander J. Boyd[3]

[1]The Johns Hopkins University, Applied Physics Laboratory, Laurel, Maryland, USA

[2]Andrews University, Berrien Spring, Michigan, USA

[3]The Aerospace Corporation, El Segundo, California, USA

Abstract. Many solar wind parameters correlate with one another, which complicates the causal-effect studies of solar wind driving of the magnetosphere. Conditional mutual information (CMI) is used to untangle and isolate the effect of individual solar wind and magnetospheric drivers of the radiation belt electrons. The solar wind density (n_{sw}) negatively correlates with electron phase space density (PSD) (average energy ~ 1.6 MeV) with time lag (τ) = 15 hr. This effect of n_{sw} on PSD has been attributed to magnetopause shadowing losses, but when the effect of solar wind velocity (V_{sw}) is removed, τ shifts to 7–11 hr, which is a more accurate time scale for this process. The peak correlation between V_{sw} and PSD shifts from τ = 38 to 46 hr, when the effect of n_{sw} is removed. This suggests that the time scale for electron acceleration to 1–2 MeV is about 46 hr following V_{sw} enhancements. The effect of n_{sw} is significant only at L* = 4.5–6 (L* > 6 is highly variable) whereas the effect of V_{sw} is significant only at L* = 3.5–6.5. The peak response of PSD to V_{sw} is the shortest and most significant at L* = 4.5–5.5. As time progresses, the peak response broadens and shifts to higher τ at higher and lower L*, consistent with local acceleration at L* = 4.5–5.5 followed by outward and inward diffusion. The outward radial diffusion time scale at L* = 5–6 is ~40 hr per R_E.

ORCID ID: 0000-0001-9342-1813

Plain Language Summary

Many solar wind parameters correlate with one another, which complicates the causal-effect studies of solar wind driving of the magnetosphere. We use conditional mutual information (CMI), which is part of information theory, to untangle and isolate the effect of individual solar wind and magnetospheric drivers of the radiation belt electrons. For example, the solar wind density negatively correlates with electron phase space density (PSD) (average energy ~ 1.6 MeV) with the response time lag of 15 hours. This has been attributed to the electron loss process called magnetopause shadowing. The time lag suggests the time scale for this process is 15 hours. However, when the effect of solar wind velocity is removed, the time lag is 7–11 hours, which is a more accurate time scale for this process. As another example, the time lag of the correlation between solar wind velocity and PSD shifts 38 to 46 hours, when the effect of solar wind density is removed. This suggests that the time scale for electron acceleration to 1–2 MeV is about 46 hours following the solar wind velocity enhancements. We also show that the effects of solar wind velocity and density have dependence on radial distance.

Keywords: radiation belt, relativistic electrons, solar wind drivers, nonlinear relationships, information theory, local acceleration, diffusion time scale, electron acceleration, magnetopause shadowing.

Index terms: 2774, 2784, 2720, 2730, 4499

Major science question:

New Science knowledge:

Broad Implications: Information theoretical tools can be useful to untangle and isolate individual solar wind and magnetospheric drivers of the radiation belt.

Key points: (1) The effect of n_{sw} on radiation belt electrons is significant only at L* = 4.5–6 and not significant at L* < 3. (2) The effect of V_{sw} on radiation belt electrons is significant at L* = 3.5–6.5 and not significant at L* < 3.5. (3) The radiation belt response time lag to V_{sw} suggests local acceleration at L* = 4.5–5.5 followed by outward and inward diffusion.

1. Introduction

The Earth's radiation belt is populated by electrons having energies of hundreds of keVs to >10 MeVs. These electrons are hazardous to satellites that encounter them in the inner-magnetosphere r ~2–8 R_E, including at the geosynchronous orbit (GEO), and at their foot points at low earth orbit (LEO) in the ionosphere, where 1 R_E = radius of the Earth = 6372 km. The MeV electrons can penetrate deep into spacecraft leading to spacecraft or instrument malfunctions while those with energies < 1 MeV can accumulate on the surface of the spacecraft bodies, leading to electrical discharges.

It has long been recognized that the variabilities of the radiation belt electrons, to a large extent, are driven by the solar wind (e.g., *Baker et al*., 1990, 2018; 2019a; *Li et al*., 2001; 2005; *Reeves*, 2007; *Ukhorskiy et al*., 2004; *Turner and Li*, 2008, *Reeves et al.*, 2013; *Xiang et al*., 2017; *Pinto et al*., 2018; *Zhao et al*., 2017, *Alves et al*., 2017). However, many solar wind parameters positively and negatively correlate with one another, which can complicate the interpretation of the solar wind drivers of the radiation belt (e.g., *Hundhausen et al*., 1970; *Wing et al*., 2016; *Wing and Johnson*, 2019; *Borovsky*, 2012; 2016; 2018; 2020; *Maggiolo et al*., 2017). For example, solar wind velocity (V_{sw}) positively correlates with radiation belt electron fluxes (J_e) (e.g., *Baker et al*., 1990; *Reeves et al*., 2011; *Balikhin et al*., 2011; *Paulikas and Blake*, 1979; *Li et al*., 2001; 2005; *Wing et al*., 2016). Solar wind density (n_{sw}) negatively correlates with radiation belt J_e (e.g., Li et al., 2005; *Lyatsky and Kazanov*, 2008a; *Kellerman and Shprits*, 2012; *Rigler et al*., 2007; *Balikhin et al*., 2011; *Wing et al*., 2016). However, V_{sw} negatively correlates with n_{sw} (e.g., *Wing et al*., 2016; *Borovsky*, 2020). This raises the question that given the V_{sw}-n_{sw} negative correlation, if V_{sw} positively correlates with radiation belt electron J_e, then the negative correlation of n_{sw} with radiation belt electron J_e may simply be coincidental. Conversely, given the solar wind property,

77 if n_{sw} negatively correlates with J_e, then the positive correlation of V_{sw} and radiation belt J_e may
78 simply be coincidental. Of course, n_{sw} and V_{sw} may independently exert influence on the radiation
79 belt electrons. In that case, how can one isolate the effect of an individual solar wind parameter?
80 A few studies attempted to separate the effects of n_{sw} from V_{sw} by using methods that bin
81 the data into small intervals of V_{sw} and n_{sw} or explicitly select events when one parameter is nearly
82 constant while the effect of the other parameter is investigated (e.g., *Lyatsky and Khazanov*,
83 2008a). This type of analysis has offered insights into the solar wind driving of the radiation belt
84 J_e. However, holding one parameter nearly constant, either explicitly or through small binning, in
85 order to investigate the second parameter does not completely eliminate the effect of the first
86 parameter. For example, selecting events when V_{sw} is nearly constant to investigate the effect of
87 n_{sw} does not completely eliminate the effect of V_{sw} because V_{sw} or its effect is not zero. Nearly
88 constant but high V_{sw} can still affect the correlation of n_{sw} and radiation belt J_e. Moreover, it does
89 not address the question of how much additional information n_{sw} provides to J_e, given V_{sw} and vice
90 versa. Many studies have shown that other solar wind parameters and magnetospheric parameters
91 can also contribute to J_e variations [e.g., *Balikhin et al*., 2011; *Rigler et al*., 2007; *Vassiliadis et*
92 *al*., 2005; *Li et al*., 2005; *Onsager et al*., 2007; *Simms et al.*, 2014;], but presently, it is not entirely
93 clear quantitatively given a main driver, e.g., V_{sw} (or n_{sw}), how much additional information these
94 parameters provide to J_e.
95 The solar wind–radiation belt systems have been shown to be nonlinear [e.g., *Wing et al*.,
96 2005; *Johnson and Wing*, 2005; *Reeves et al*., 2011; *Kellerman and Shprits*, 2012; *Wing et al*.,
97 2016]. For nonlinear system, linear correlational analysis can be misleading [e.g., *Balikhin et al*.,
98 2010; 2011].
99 Information theory has been shown to be quite useful for studies of the Earth's

magnetosphere (*Balasis et al*., 2008; 2009; 2011; 2013; *Stumpo et al*., 2020; *Materassi et al*., 2011, *De Michelis et al*., 2011, 2017; *March et al*., 2005; *Johnson and Wing*, 2005; 2014, *Wing et al*., 2016; *Johnson et al*., 2018; *Wing and Johnson*, 2019; *Runge et al*., 2018; *Papadimitriou et al*., 2020; *Manshour et al*., 2021), Kronian magnetosphere (*Wing et al*., 2020), and the Sun (*Consolini et al*., 2009; *Wing et al.*, 2018; *Snelling et al*., 2020). Information theory can help identify nonlinearities in the system and information transfer from one variable to another. Moreover, information theory can also help untangle the drivers that are positively or negatively correlated with one another (*Wing et al., 2016*; *Wing and Johnson*, 2019).

Wing et al. (2016) used information theoretic tools to study the solar wind driving of the radiation belt electrons. The study used the publicly available Los Alamos National Laboratory (LANL) satellite data, which provide geosynchronous electron flux measurements at daily resolution. When the study began in early 2015, the Radiation Belt Storm Probes (RBSP) or Van Allen Probes satellites had only been operational for a few years, and there was not enough data for a statistical study. Usage of the daily resolution of the radiation belt electron data prevented *Wing et al*. (2016) from resolving any electron response lag time to the solar wind drivers that is shorter than 24 hours. For example, the LANL MeV electron J_e negatively correlates with daily averaged n_{sw} with a lag time (τ) of 1 day. Zhao et al. (2017) correlated daily averaged radiation belt electron phase space density (PSD) with n_{sw} and also obtained τ = 1 day for MeV electrons (μ > 700 MeV G–1). However, if the effect of V_{sw} is properly removed, τ shifts to 0 day (*Wing et al*., 2016). In other words, the radiation belt electron response to n_{sw} is less than 24 hr. However, the study could not pinpoint exactly how much less than 24 hr with the daily resolution LANL data. Another limitation of *Wing et al*. (2016) study is that the LANL data only provide the electron observations at a fixed radial distance from the Earth, at the geosynchronous orbit.

Since *Wing et al.* (2016) study, RBSP has gathered seven years of radiation belt electron data (2013-2019) at high time resolution (< 1 min) from $2 < L^* < 7$. Hence, the time is ripe for a follow up study that uses the RBSP data. As in *Wing et al*. (2016), the present study uses information theory to determine the solar wind and magnetospheric drivers of the radiation belt electrons and the response time scales. In order to focus on the drivers of the nonadiabatic heating and acceleration, the present study examines the response of the radiation belt electron phase space density (PSD) to the drivers.

2. Data set

Van Allen Probe (or RBSP) mission, which was launched in 2012, had two identically instrumented spacecraft in near-equatorial orbit (about 10° inclination) with perigee at 600 km altitude and apogee at 5.8 R_E geocentric (*Mauk et al.*, 2013). The MAGnetic Electron Ion Spectrometer (MagEIS) and Relativistic Electron-Proton Telescope (REPT) instruments are part of the Energetic particle, Composition, and Thermal plasma Suite (ECT) instrument on board of RBSP (*Spence et al.,*, 2013). MagEIS measured the energy range of 30 keV to 4 MeV for electrons and 20 keV to 1 MeV for ions (*Blake et al*., 2013) while REPT measured electrons with energy range 1.5 to ≥ 10 MeV and protons with energy range 20 to 75 MeV (*Baker et al*., 2012).

The present study focuses only on the electron data. Radiation belt electron dynamics can often be described by their adiabatic invariants and PSD (μ, K, L*) where μ = the first adiabatic invariant related to the gyromotion perpendicular to the magnetic field line, K = the second adiabatic invariant related to the bounce motion along the field line, and L or L* = the third adiabatic invariant related to the curvature and gradient drift motion around the Earth (actually L* is inversely proportional to the third invariant Φ) (*Roederer*, 1970; *Schulz and Lanzerotti*, 1974;

Lejosne and Kollman, 2020).

Data from the RBSP-ECT Combined dataset (Boyd et al., 2021) are used to obtain electron PSD as a function of adiabatic invariants across the full MagEIS and REPT energy range. The PSD is calculated using the techniques outlined in (*Turner et al.*, 2014a; 2014b; *Boyd et al*., 2014) at ~5 min time cadence. We select the electrons with μ = 725–875 MeV G^{-1} and K = 0.09–0.13 R_E $G^{-0.5}$. These electrons have an average energy of ~1.6 MeV, but they range from 480 keV to 4.8 MeV spanning over L* of 2.5 to 6.8.

The solar wind, AL, and SYM-H data 2013-2019 come from OMNI 1 min resolution data provided by NASA (http://omniweb.gsfc.nasa.gov/). Both the PSD and OMNI data 2013-2019 are averaged with 30 min sliding window.

We merge each OMNI solar wind parameter (V_{sw}, n_{sw} etc.) with the RBSP electron PSD. As described in Section 3, we perform time shifted correlation and conditional mutual information analysis to determine the radiation belt electron response lag time up to 120 hr. Depending on the solar wind parameter, typically the merged datasets have approximately 60,000 to 85,000 points.

3. Methodology

Mutual information and conditional mutual information are briefly described below, but they are also described in *Balasis et al*. (2013), and *Wing et al*. (2016, 2018).

Mutual information (MI) (*Tsonis*, 2001; *Li*, 1990; *Darbellay and Vajda*, 1999) between two variables, *x* and *y*, compares the uncertainty of measuring variables jointly with the uncertainty of measuring the two variables independently. The uncertainty is measured by Shannon entropy. In order to construct the entropies, it is necessary to obtain the probability distribution functions, which in this study are obtained from histograms of the data based on discretization of the variables

(i.e. bins).

Suppose that two variables, x and y, are binned so that they take on discrete values, $\hat{x}$ and $\hat{y}$, where

$$x \in \{\hat{x}_1, \hat{x}_2, \cdots, \hat{x}_n\} \equiv \aleph_1; \quad y \in \{\hat{y}_1, \hat{y}_2, \cdots, \hat{y}_n\} \equiv \aleph_2 \qquad (1)$$

The variables may be thought of as letters in alphabets $\aleph_1$ and $\aleph_2$, which have n and m letters, respectively. The extracted data can be considered as sequences of letters. The entropy associated with each of the variables is defined as

$$H(x) = -\sum_{\aleph_1} p(\hat{x}) \log p(\hat{x}) ; \qquad H(y) = -\sum_{\aleph_2} p(\hat{y}) \log p(\hat{y}) \qquad (2)$$

where $p(\hat{x})$ is the probability of finding the word $\hat{x}$ in the set of x-data and $p(\hat{y})$ is the probability of finding word $\hat{y}$ in the set of y-data. To examine the relationship between the variables, we extract the word combinations $(\hat{x}, \hat{y})$ from the dataset. The joint entropy is defined by

$$H(x,y) = -\sum_{\aleph_1 \aleph_2} p(\hat{x},\hat{y}) \log p(\hat{x},\hat{y}) \qquad (3)$$

where $p(\hat{x},\hat{y})$ is the probability of finding the word combination $(\hat{x},\hat{y})$ in the set of (x, y) data.

The mutual information is then defined as

$$\mathrm{MI}(x, y) = \mathrm{H}(x) + \mathrm{H}(y) - \mathrm{H}(x, y) \qquad (4)$$

While MI is useful to identify nonlinear dependence between two variables, it is often useful to consider conditional dependency with respect to a conditioner variable z that takes on discrete values, $\hat{z} \in \{ z_1, z_2, \ldots . z_n\} \equiv \aleph_3$. The conditional mutual information (*Wyner*, 1978)

$$\mathrm{CMI}(x, y \mid z) = \sum_{\aleph_1 \aleph_2 \aleph_3} p(\hat{x},\hat{y},\hat{z}) \log \frac{p(\hat{x},\ \hat{y} \mid \hat{z})}{p(\hat{x} \mid \hat{z})\, p(\hat{y} \mid \hat{z})} = \mathrm{H}(x,z) + \mathrm{H}(y,z) - \mathrm{H}(x,y,z) - \mathrm{H}(z) \qquad (5)$$

determines the mutual information between x and y given that z is known. In the case where z is unrelated, $\mathrm{CMI}(x, y| z) = \mathrm{MI}(x,y)$, but in the case that x or y is known based on z, then $\mathrm{CMI}(x,y|z) = 0$. CMI therefore provides a way to determine how much additional information is known given another variable. CMI can be seen as a special case of the more general conditional redundancy

192 that allows the variable z to be a vector (e.g., *Prichard and Theiler*, 1995; *Johnson and Wing*,
193 2014).

194 Herein, we use the short hand Pearson's linear correlation corr($x(t)$, $y(t + \tau)$) as corr($x \rightarrow$
195 y). Likewise, CMI($x(t)$, $y(t + \tau)| z(t)$) is denoted as CMI($x \rightarrow y| z$). We define i_{tr} = information
196 transfer = CMI($x \rightarrow y| z$) – mean noise, where noise = CMI(sur(x) $\rightarrow y| z$), sur(x) is the surrogate
197 data of x and is obtained by randomly permuting the order of the time series of array x. Mean and
198 σ of the noise are calculated from an ensemble of 100 values of CMI(sur(x) $\rightarrow y| z$). The mean
199 noise and σ estimate are valuable diagnostics included on all of the CMI data presented here: any
200 CMI outside the 3σ noise range are significant and CMI less than the 3σ from the noise is
201 considered not significant. Furthermore, we define $i_{tr\_max} = i_{tr}$ at the peak τ and significance =
202 i_{tr}/σ.

203

204 **4. Applying information theory to radiation belt MeV electron data**

205 **4.1 A simple example of an application of conditional mutual information (CMI)**

206 CMI can be quite useful to untangle the effects of multiple drivers of a system. Figure 1
207 presents a simple example that illustrates this point. Figure 1a plots corr($V_{sw} \rightarrow$ PSD). The figure
208 shows that V_{sw} positively correlates with PSD and the correlation peaks at τ = 38 hr. The
209 correlation is significant with n = 84,729 points and correlation coefficient (r) = 0.47 and $p < 0.01$.
210 Previous studies have also found good correlations between V_{sw} and radiation belt electrons with
211 ~2 days lag and the lag time has been attributed to the time scale to accelerate the electrons to 1–
212 2 MeV due to local acceleration, radial transport, or some other acceleration mechanisms (e.g.,
213 *Baker et al*., 1990; *Shprits et al.*, 2008; 2009; *Reeves et al*., 2011; 2013; *Li et al*., 2005; *Ukhorskiy*
214 *et al*., 2005; *Wing et al.*, 2016; *Summers et al*., 2007; *Thorne et al*., 2013; *Newell et al*., 2016;

215 *Turner and Li*, 2008; *Boyd et al.*, 2016; 2018). Figure 1b plots the corr($n_{sw} \rightarrow$ PSD), which shows
216 that n_{sw} negatively correlates with PSD with a minimum at τ = 15 hr, r = –0.22, n = 84,729, $p <$
217 0.01. *Lyatsky and Khazanov* (2008a) also found the same negative correlation at τ = 15 hr. The
218 negative correlation has been previously attributed to the magnetopause shadowing effect: an
219 increase in n_{sw} would increase solar wind dynamic pressure (P_{dyn}), which would compress the
220 magnetosphere leading to radiation belt electron losses (e.g., *Li et al.*, 2001; *Kellerman and*
221 *Shprits*, 2012; *Turner et al*., 2012; *Ukhorskiy et al*., 2006). Figure 1c plots the corr($P_{dyn} \rightarrow$ PSD),
222 which shows that the radiation belt electron response to P_{dyn}, which is ~ n_{sw} V_{sw}^2, has dual modes.
223 At small τ, τ < ~20 hr, P_{dyn} negatively correlates with PSD, which is similar to the effect of n_{sw}
224 and can be attributed to the magnetopause shadowing effect. However, at large τ, τ > 40 hr, P_{dyn}
225 positively correlates with PSD, which is similar to the effect of V_{sw}. The correlations are significant
226 at p < 0.01 and n = 82,652. Zhao et al. (2017) correlated P_{dyn} with PSD at daily time resolution
227 and also found a dual response mode of the PSD to P_{dyn}. Figure 1d plots CMI($P_{dyn} \rightarrow$ PSD| n_{sw}),
228 which shows the dependence of PSD on P_{dyn}, given n_{sw}. It shows that if we remove the effect of
229 n_{sw}, the effect of P_{dyn} on PSD is similar to that of V_{sw} in Figure 1a, as expected. The CMI curve
230 does not match exactly the correlation curve in Figure 1a because the CMI curve takes into account
231 the nonlinearities in the data.

232 In Figure 1d, the green solid and dashed curves are mean noise and 3σ from the noise,
233 respectively. The significance at peak τ = 51 hr is 203σ and hence it is significant.

234

235 **4.2 Isolating the effects of the solar wind velocity from density and vice versa**

236 *Wing et al*. (2016) isolated the effects of V_{sw} and n_{sw} on the radiation belt electron J_e using
237 CMI. They found that CMI($V_{sw} \rightarrow J_e$| n_{sw}) peaks at τ = 2-3 days while CMI($n_{sw} \rightarrow J_e$| V_{sw}) peaks

238 at $\tau = 0$ day. However, the lag times, τ, in *Wing et al*. (2016) are imprecise due to the usage of the
239 daily resolution LANL electron data. Furthermore, LANL data are limited to GEO, but the outer
240 belt is not accurately represented by data at GEO alone, especially for the heart of the outer belt
241 between $4 \leq L \leq 5$ (e.g., *Baker et al*., 2019b). In the present study, we recompute the CMIs using
242 30 min resolution RBSP PSDs representative of ~1 MeV electrons throughout the entire outer belt
243 and solar wind data. Furthermore, by using electron PSD for fixed values of the first and second
244 adiabatic invariants in place of J_e as a function of energy, the data used here further deconvolute
245 the energy and pitch angle dependencies of the underlying physical processes that drive radiation
246 belt enhancements and losses.

247 Figures 2a and 2b replot corr($V_{sw} \rightarrow$ PSD) and corr($n_{sw} \rightarrow$ PSD), which are plotted in
248 Figures 1a and 1b, respectively. However, V_{sw} negatively correlates with n_{sw} and corr($V_{sw} \rightarrow n_{sw}$)
249 has a minimun at τ = 15 hr ($r = -0.48$, n = 105,459, $p < 0.01$), as shown in Figure 2c. For
250 completeness, Figure 2c also plots corr($n_{sw} \rightarrow V_{sw}$) (red curve), which has $r = 0.10$, $p < 0.01$. The
251 figure shows that $|\text{corr}(V_{sw} \rightarrow n_{sw})| > |\text{corr}(n_{sw} \rightarrow V_{sw})|$. The negative correlation between V_{sw} and
252 n_{sw} have been previously reported with similar τ (e.g., *Wing et al*., 2016; *Maggiolo et al*., 2017;
253 *Borovsky*, 2020). Note that τ may vary from year to year (*Wing et al*., 2016), leading to an overall
254 broadening of the peak when considering an ensemble of intervals across the solar cycle.

255 Given that V_{sw} negatively correlates with n_{sw}, if n_{sw} negatively correlates with PSD (Figure
256 2b), then the positive correlation between V_{sw} and PSD may be deemed just coincidental. To check
257 on this possibility, we compute CMI($V_{sw} \rightarrow$ PSD| n_{sw}), which is plotted in Figure 2d. The figure
258 shows that even after the effect of n_{sw} has been removed, there is still strong information transfer
259 from Vsw to PSD, which peaks at τ = 46 hr (n = 78,811, significance = 378σ). Apparently,
260 removing the effect of n_{sw}, shifts the peak to the right. The lag time of τ = 46 hr obtained from

CMI is considered a more accurate radiation belt electron response time to the V_{sw} (the time scale for electron acceleration to 1-2 MeV energy range) than the lag time of τ = 38 hr obtained from Pearson's correlation.

We can also check whether or not corr($n_{sw} \rightarrow$ PSD) is coincidental, given the V_{sw} negative correlation with n_{sw} and V_{sw} positive correlation with PSD. Figure 2e plots CMI($n_{sw} \rightarrow$ PSD$|$ V_{sw}), which shows two peaks. The primary peak at τ = 7–11 hr (n = 78,811, significance = 52σ) can be compared to the minimum in corr($n_{sw} \rightarrow$ PSD) in Figure 2b. Apparently, removing the effect of V_{sw}, shifts the peak to the left. The lag time of τ = 7–11 hr is considered a more accurate radiation belt electron response time to the magnetopause shadowing effect than the τ = 15 hr obtained from the correlational analysis. Note that CMI only gives positive values and does not distinguish negative from positive correlations. As such, CMI is analogous to $|r|$.

Figure 2e shows that there is a secondary broad peak at τ = 80–120 hr (or even larger). Unlike the primary peak, which is a negative correlation, the secondary peak is a positive correlation with n_{sw}. In order to show this, we plot PSD(t + τ) vs. V_{sw}(t) vs. n_{sw}(t) for τ = 0, 5, 10, 40, 80, 100, and 120 hr in Figure 3 panels a to g, respectively. In all panels, it can be seen that at high V_{sw}, V_{sw} > ~500 km s^{-1}, V_{sw} positively correlates with the radiation belt electron PSD as previously reported (*Reeves et al*., 2011; *Li et al*., 2001; *Kellerman and Shprits*, 2012; *Wing et al*., 2016). However, for V_{sw} < ~450 km s^{-1}, and small τ (τ = 0, 5, and 10 hr), n_{sw} negatively correlates with the radiation belt electron PSD, which is consistent with the first and primary peak of CMI($n_{sw} \rightarrow$ PSD$|$ V_{sw}) in Figure 2e, which can be attributed to the magnetopause shadowing effect. At τ = 40 hr, there is little or no correlation between n_{sw} and the PSD, which is consistent with the minimum of CMI($n_{sw} \rightarrow$ PSD$|$ V_{sw}) in Figure 2e. However, at large τ, τ = 80, 100, 120 hr and V_{sw} < ~450 km s^{-1}, n_{sw} positively correlates with PSD, which is consistent with the secondary peak in

Figure 2e. This positive correlation between n_{sw} and electron PSD at large τ cannot be seen in the corr(n_{sw} → PSD) in Figure 2b because the effect has been smeared or cancelled out by the effects for all V_{sw} where high electron PSD can correspond to high and low n_{sw} (Figure 3 panels e–g).

It is not clear what causes the positive linear and nonlinear correlation between n_{sw} and electron PSD at large τ. n_{sw} may be a proxy for another parameter. As an example, n_{sw} positively correlates with |IMF B| (peak τ = 6 hr, r ~ 0.40, n = 105,923, $p < 0.01$) as plotted in Figure 4a, which has implications for the radiation belt electrons. This correlation has been previously observed (*Borovsky*, 2020; *Maggiolo et al*., 2017). Larger n_{sw} would correspond to more negative IMF B_z when IMF B_z is southward (IMF $B_z < 0$) and more positive IMF B_z when IMF B_z is northward (IMF $B_z > 0$), as shown in Figures 4b and 4c, respectively. Figure 4b shows that n_{sw} negatively correlates with southward IMF (peak τ = 6 hr, r = 0.3, n = 54,265, $p < 0.01$) while Figure 4c shows that n_{sw} positively correlates with northward IMF (peak τ = 8 hr, r = 0.3, n = 51,388, $p < 0.01$). The n_{sw} negative correlation with IMF $B_z < 0$ would be relevant to the discussion of the effect n_{sw} on the radiation belt electrons because prolonged southward IMF can lead to subtorms (e.g., *Birn and Hones*, 1981; *Rostoker*, 1983; *McPherron et al*., 1986; *McPherron*, 1991; *Lui*, 1991; *Lyons*, 1995; *Lyons et al*., 1997; *Johnson and Wing*, 2014; *Birn et al*., 1997; 2006), which in turn can lead to injections of seed electrons, enhanced chorus wave activity, and the growth of the MeV radiation belt electrons (e.g., Miyoshi et al., 2013; Jaynes et al., 2015; see Section 5.3).

n_{sw} may also be correlated or be a proxy for other solar wind parameters. For example, *Kepko et al*. (2019) reported that a sharp density increase can be accompanied by quasiperiodic density fluctuations that can lead to the growth of the globally coherent magnetospheric ultralow frequency (ULF) waves, which can, in turn, accelerate radiation belt electrons (e.g., *Matthie and*

307 *Mann*, 2000; *O'Brien et al*., 2003; *Ukhorskiy et al*., 2005; *Hudson et al*., 2008; *Li et al*., 2009;
308 *Mann et al*., 2016; *Zhao et al*., 2018; *Jaynes et al*., 2018). Hence, the long range correlation of
309 (n_{sw}, PSD) and (IMF $B_z > 0$, PSD) may be attributed to the density fluctuations and ULF waves.
310 Whatever the mechanism is, our result shows that the time scale for such process to energize
311 electrons to 1–2 MeV is slow, > 70 hr.
312
313 **4.3 The radial dependence of the radiation belt electrons on the solar wind density and**
314 **velocity**
315 The effects of the n_{sw} and V_{sw} on the radiation belt electrons have a dependence on the
316 radial distance or L* (e.g., *Baker et al*., 2019a; *Tang et al*., 2017a; *Turner et al*., 2019; *Zhao et al*.,
317 2017; *W. Li et al*., 2014). In order to show this, PSD data are binned from L* = 3 to 6.5 into 7 bins
318 with bin width = 0.5. The data coverage for the electrons with μ = 725–875 MeV G^{-1} and K =
319 0.09–0.13 $R_E\, G^{-0.5}$ is poor for L* < 3 and L* > 6.5. Figure 5 shows corr($n_{sw} \rightarrow$ PSD) as a function
320 of L*. It shows that the correlation is near 0 at L* = 3–3.5, but slowly decreases with increasing
321 L*. Except for L* = 3–3.5 (n = 8435, Figure 5a), the correlations are significant ($p < 0.01$) at the
322 minimum τ (τ = 15, 16, 17, 17, 17, 13 hr), r = (–0.086, –0.17, –0.27, –0.31, –0.34, –0.50), (n =
323 8,302, 11,481, 17,7891, 27,060, 6,236, 528) for panels (b–g), respectively. The number of points
324 in L* = 6–6.5 (Figure 5g) is the fewest, which results in a noisier correlation. However, as
325 discussed in the Sections 1, 4.1, and 4.2, the correlation may be inaccurate because n_{sw} negatively
326 correlates with V_{sw} (Figure 2c) and the system is nonlinear (Wing et al., 2016). Hence, we calculate
327 CMI($n_{sw} \rightarrow$ PSD| V_{sw}) for the PSD data in the same bins. The results are plotted in Figure 6. The
328 figure shows that the effect of n_{sw} on PSD is at the noise level at L* = 3–4.5, is significant at L* =
329 5–6, and back to the noise level at L* = 6–6.5. However, the result for L* = 6–6.5 is considered

not reliable because of the small number of points (n = 528). The response lag times based on the first peak are τ = 9, 10, and 7 hr (n = 16,629, 25,238, and 5865; significance = 17, 42, and 5 σ) at L* = 4.5–5, 5–5.5, and 5.5–6, respectively. Notice that the response lag times are quite different in Figures 5 and 6.

For completeness, we examine the effect of P_{dyn} on the PSD. Figure 7 plots CMI($P_{dyn} \rightarrow$ PSD| V_{sw}) as a function of L* in the same format as Figure 6. It shows that the effect of P_{dyn} on PSD is similar to that of n_{sw}, as expected. The largest effect of P_{dyn} on electron PSD can be found at L* = 4.5–6. (significance = 32, 53, 17 σ for L* = 4.5–5, 5–5.5, and 5.5–6), respectively. The number of points in each bin in Figure 6 is the same as that in Figure 7. Taken together, Figures 6 and 7 suggest that the magnetopause shadowing is effective only at L* = 4.5–6. At L* = 6–6.5, there is a high variability of PSD and the bin has fewest number of points and hence the result is inconclusive.

Moreover, the significances are higher for the first peak in Figure 7 panels d–f than their counterparts for CMI($n_{sw} \rightarrow$ PSD| V_{sw}) in Figure 6 panels d–f, suggesting that the real causal parameter for the magnetopause shadowing is P_{dyn} rather than n_{sw}. However, the opposite is true for the secondary peak. This would suggest that the secondary peak may be more causally related to n_{sw} (or its proxy) than P_{dyn}.

We perform the same analysis with V_{sw} and electron PSD. Figure 8 shows corr($V_{sw} \rightarrow$ PSD) as a function of L* in the same format as Figure 5. The correlations are all significant at $p < 0.01$ at the maximum τ (τ = 40–120, 30–120, 38, 30, 37, 45, 30–90 hr), (r = 0.14, 0.27, 0.42. 0.57, 0.62, 0.64, 0.70) for L* = 3–3.5, 3.5–4, 4.–4.5, 4.5–5, 5–5.5, 5.5–6, and 6–6.5, respectively. Baker et al. (2019a) also found higher correlation with increasing L (r = 0.32, 0.51, and 0.61 for L = 3.5, 4.5, and 5.5, respectively). For comparison, Figure 9 plots CMI($V_{sw} \rightarrow$ PSD| n_{sw}) as a function of

L* in the same format as Figure 6. The number of points in each bin is the same as that in Figure 6. Figure 9 shows that the CMI is at the noise level at L* = 3–3.5 (panel a), unlike its counterpart in Figure 8a. At L* = 3.5–4.5, the CMI has a broad peak from $\tau \sim 50$–100 hr (or larger for the case L* = 3.5–4) and the peaks are significant (peak significance = 18 and 46 σ for L* = 3.5–4 and 4–4.5), respectively. At L* = 4.5–6, the CMI peaks are narrower (peak τ = 40, 46, 57 hr; significance = 236, 399, and 100 σ), respectively. Interestingly, at τ = 6–6.5, the peak broadens again but remains significant (peak significance = 19 σ). To help visualize the evolution of the CMI, red dashed vertical lines at τ = 40 hr is drawn in Figure 9.

The radiation belt electron response lag times as a function of L* is further examined in Figure 10. The figure shows the normalized i_{tr} for each L* bin (the blue curve subtracted by the solid green curve in Figure 9). The orange and yellow color correspond roughly to the top 20% of i_{tr} in each L* bin. At L* = 4.5–5.5, response lag time peaks around τ = 35–50 hours, which is consistent or close to the previously reported time scale of 2 days to accelerate electrons to 1-2 MeV (*Paulikas and Blake*, 1979; *Reeves et al*., 2011; *Li et al*., 2001; *Wing et al*., 2016). At higher L*, L* = 5.5–6, the peak broadens and shifts to larger τ, τ = 45–65 hr. At L* = 6–6.5, the peak is even broader at τ = 40–100 hr. At lower L*, L* = 4–4.5 and 3.5–4, one can also see successive broadening of the peak as the peak shifts to larger τ, τ = 35–55 hr and τ = 45–60 hr, respectively.

Our result is consistent with local acceleration where the peak of the electron acceleration region is located at L* = 4.5–5.5, from where electrons diffuse outward and inward (Section 5.3). This scenario would be consistent with the *O'Brien et al*. (2003) study that found the peak of the 1.5 MeV electron microburst precipitation is located at L = 4.5. It would also be consistent with the *Green and Kivelson* (2004) study that found evidence for local acceleration near L* = 5. More recently, in the RBSP era, Tang et al. (2017a) found that the peak flux of 1 MeV electrons is

located mostly at L ~ 4–5 in 74 storm events and they also found evidence for local acceleration. *Boyd et al*. (2018) found the peak PSD is located mostly at L* = 4.5 – 5.5 in 80 storm events. They concluded that 70 out of 80 events show evidence of local acceleration based on the PSD vs. L* spectra. These results are consistent with our interpretation of Figures 9 and 10 that the L* band with the information peak at the smallest τ corresponds to the local acceleration region. The shifting of the peak to a larger τ at higher or lower L* suggests outward or inward diffusion, respectively.

However, there is also evidence that suggests localized acceleration in tandem with outward or inward diffusion originating from L* = 4.5–5.5 (e.g., Allison and Shprits, 2020). For example, at L* = 4–4.5, one can see that the i_{tr} starts increasing at τ = 25 hr, very much about the same time i_{tr} increases at L* = 4.5–5.5 hr, but the significance is lower (Figure 9). This may suggest that the whistler mode chorus waves are also present at L* = 4–4.5 and not all 1–2 MeV electrons are transported from L* = 4.5–5.5. The same dynamics can be seen at the outermost L*, L* = 6–6.5.

The radial diffusion time scale can be estimated from the peak τ at each L* band. In Figure 10, the peak τ increases from ~ 40 hr at L* = 4.5–5.5 to ~60 hr at L* = 5.5–6, suggesting outward diffusion time scale of 40 hr per R_E. The diffusion time scale of 40 hr (or about 2 days) per R_E can be compared with the theoretical estimate of 1–6 days that is attributed to ULF waves at L* = 6 (e.g., *Elkington et al*., 2003).

4.4 The dependence of the radiation belt electrons on the magnetospheric state

So far we have analyzed the dependence of the radiation belt electron PSD on the solar wind drivers, specifically V_{sw}, n_{sw}, and P_{dyn}. However, the radiation belt electrons depend not just

399 on the external (solar wind) drivers but also the internal state of the magnetosphere (e.g., *Reeves*
400 *et al*., 1998; *Baker et al.*, 2019a; *Lyatsky and Khazanov*, 2008b; *Borovsky and Denton*, 2014; *Tang*
401 *et al*., 2017b; *Borovsky*, 2017; *Zhao et al*., 2017). In order to determine how the radiation belt
402 electrons depend on the internal state of the magnetosphere, we examine the relationships of the
403 electron PSD with AL and SYM-H indices. SYM-H index gives a measure of the strength of the
404 ring current and storm (*Iyemori*, 1990) while AL gives a measure of the strength of the westward
405 auroral electrojets and substorm (*Davis and Sugiura*, 1966). SYM-H is similar to Disturbance
406 Storm Time (Dst) index (*Dessler and Parker*, 1959), except that SYM-H index is defined to have
407 a one minute time resolution whereas Dst index has one hour resolution. Both SYM-H (proxy for
408 storms) and AL (proxy for substorms) can be associated with plasma injections to the inner
409 magnetosphere, which can enhance the whistler mode chorus waves and provide the seed
410 population for the local acceleration (*Katus et al*., 2013; *Wing et al*., 2014).

411 Figure 11a plots corr(AL $\rightarrow$ PSD), which shows that AL negatively correlates with electron
412 PSD with a minimum $\tau \sim 53$ hr ($n = 70{,}125$, $r = -0.33$, $p < 0.01$). Note that a smaller (more
413 negative) AL corresponds to a more intense substorm and larger auroral electrojets. Figure 11b
414 plots corr($V_{sw} \rightarrow$ PSD) (same as Figure 1a). Figure 11c plots corr($V_{sw} \rightarrow$ AL), which shows that
415 the auroral electrojet response to V_{sw} is fairly quick $\tau = 0$ hr (< 30 min) ($n = 82{,}995$, $r = -0.40$, $p <$
416 0.01). Similar correlation was obtained by *Smirnov et al*. (2020). Given the positive correlation
417 of V_{sw} and electron PSD, and the negative correlation of V_{sw} and AL, one may ask the question
418 whether the negative correlation between AL and electron PSD may just simply be coincidental or
419 whether AL can independently affect PSD. Figure 11d plots CMI(AL $\rightarrow$ PSD| V_{sw}), which shows
420 that the radiation belt electrons still have strong dependence on AL even after the effect of V_{sw} has
421 been removed. The CMI peaks at $\tau \sim 50$–80 hr (significance = 58σ, $n = 64{,}564$), suggesting that

perhaps the time scale to accelerate electrons to 1–2 MeV energy range from the time of substorm onset or substorm particle injection is about 50–80 hr. This time scale is an ensemble average for all L*. To help visualize the comparison of Figures 11a and 11d, a dashed vertical red line is drawn at τ = 53 hr (the minimum of corr(AL $\rightarrow$ PSD)). It shows that removing the effect of V_{sw}, shifts the peak to the right (to a larger τ) by a little bit (~10 hr).

Figure 12 displays the normalized i_{tr} as a function of L* and τ where i_{tr} = CMI(AL $\rightarrow$ PSD| V_{sw}) – mean noise in the same format as Figure 10. The i_{tr} is at the noise level at L* = 3–3.5 (n = 6409). At L* = 6–6.5, there is a high variability in PSD and the bin has the fewest number of points (n = 216) and hence the result is unclear and not shown. The region with the largest significance is L* = 4.5–5 and 5–5.5 with peak τ = 40–80 and 45–85 hr and peak significance = 33 and 38 σ (n = 13,825 and 20,527) respectively. The peak shifts to larger τ, τ = 75–100 hr, at L* = 5.5 –6 (n = 4686, peak significance = 18σ), suggesting outward diffusion from L* = 4.5–5.5. At L* = 4–4.5, the peak is broad, τ = 35–80 hr (n = 8802; peak significance = 19 σ). It is not clear what causes this broad peak. Because the peak starts at the same time or even earlier than at L*=4.5–5.5, it may suggest the whistler wave activity is present nearly simultaneously from L* = 4–5.5. However, the peak seems to decay slowly suggesting perhaps inward diffusion or longer lasting wave activity at L* = 4–4.5. At L* = 3.5–4, the peak is broad at τ = 60–110 hr, but the peak significance is relatively small (n = 6379, peak significance = 9 σ), which would be consistent with inward diffusion from higher L*.

Iles et al. (2006) examined a substorm event and found that peak PSD for electrons > 0.8 MeV is located at L* = 4.3–5.5, which is close to the L* band with the largest CMI significance, L* = 4.5–5.5. They also found evidence of local acceleration and radial diffusion.

We perform similar analysis with SYM-H. Radiation belt electrons have been found to

show great variabilities during storms (e.g., *Reeves et al*., 2003; *Turner et al*., 2019; *Baker et al*., 2019a). Figure 13 is similar to Figure 11, except that it is for SYM-H instead of AL index. Figure 13a plots corr(SYM-H $\rightarrow$ PSD), which shows that SYM-H negatively correlates with electron PSD with a minimum at $\tau \sim 40$ hr (n = 91,589, r = –0.35, $p < 0.01$) while Figure 13b plots corr($V_{sw} \rightarrow$ PSD) (same as Figure 11b). V_{sw} negatively correlates with SYM-H and the correlation has a minimum at τ = 2–4 hr (n = 91,589, r = –0.35, $p < 0.01$) (Figure 13c), suggesting that the ring current response to V_{sw} has a lag time of about 2–4 hr. Similar correlation was obtained in previous studies (e.g., *Maggiolo et al*., 2017). Figures 13 a–c pose the same dilemma as Figures 11 a–c do for AL. That is, given the positive correlation of V_{sw} and electron PSD and the negative correlation of V_{sw} and SYM-H, one may ask whether the negative correlation of SYM-H and PSD could just simply be coincidental or whether SYM-H provides additional information about PSD. Figure 13d plots CMI(SYM-H $\rightarrow$ PSD| V_{sw}), which shows that SYM-H indeed provides additional information to electron PSD even after the effect of V_{sw} has been removed. The CMI peaks at $\tau \sim$ 30–70 hr (n = 84,729, significance = 109 σ), suggesting that perhaps the time scale to accelerate electrons to 1–2 MeV energy range from the time of ring current enhancement is about 30–70 hr. However, the effect of SYM-H has a dependence on radial distance, as discussed next.

Figure 14 plots i_{tr} as a function of L* where i_{tr} = CMI(SYM-H $\rightarrow$ PSD| V_{sw}) – mean noise in the same format as Figure 12. The figure suggests a complicated relationship between SYM-H and radiation belt electrons. At L* = 6–6.5, i_{tr} is at the noise level, which can be attributed to high PSD variabilities as well as small number of points (n = 336). Studies found that storms can increase, decrease, or have little effect on radiation belt electron fluxes at geosynchronous orbit (e.g., *O'Brien et al*., 2001; *Reeves et al*., 2003). An increase in SYM-H (or ring current) would decrease magnetospheric |B| by greater proportion with increasing L* because magnetospheric |B|

decreases with r^{-3} (e.g., *Turner et al*., 2012). The effect of the reduction in |B| would be a decrease in PSD due to the outward transport because of the third adiabatic invariant. This Dst or SYM-H effect would counter the effect of the PSD enhancement due to the storm plasma injection and the ensuing local acceleration.

The highest peak significance can be found at L* = 5 – 5.5 (peak τ = 20–55 hr, significance = 79σ, n = 27,060). The peak shifts to higher τ at higher L*, suggesting outward diffusion. At L* = 5.5–6, the peak can be found at τ = 60–75 hr (n = 6236, peak significance = 26 σ). At L* = 4–4.5 and 4.5–5, the i_{tr} peaks at τ = 30–60 and 30–75 hr (n = 11,495 and 17,924; peak significance = 38 and 47 σ, respectively). The large i_{tr} at L* = 4–5 would be roughly consistent with *Tang et al*. (2017a), which found that the peak flux of 1 MeV electron at L = 4–5 in 74 storm events and with *Green and Kivelson* (2004), which found local acceleration at L* = 5.

At L* = 3.5–4, the peak is very broad at τ = 20–120 hr or even higher (n = 8317, peak significance = 23 σ). It is not clear what causes such a broad peak. The response at τ < 30 hr suggests that the 1-2 MeV electrons at this time could not have originated from higher L* shell. Thus, it may suggest the presence of wave activity at this L* band. On the other hand, the response at τ > 80 hr, may suggest inward diffusion from higher L* shell or long-lasting wave activity. At L* = 3–3.5, the CMI peaks at τ = 110–120 hr or even higher (n = 8435, peak significance = 14). The analysis stops at τ = 120 hr. The large τ may suggest slow diffusion from outer L* shell. The slow diffusion at small L* would be consistent with the expected radial diffusion time scale that increases with decreasing |B| and L*, but this needs to be investigated further. It is worth noting that out of all the parameters that we have examined, only SYM-H can provide information about radiation belt electron PSD at L* = 3–3.5 albeit only a small amount. The CMI at L* = 3–3.5 and τ < 100 hr is low, which is consistent with *Turner et al*. (2019) study that found storms have little

491 effect on 1–2 MeV electrons at L < 3.5 (see their Figure 2), but apparently at τ > 100 hr, the storm
492 effect is significant but only moderately.

493 The complicated response of the radiation belt to SYM-H or storm can be attributed to
494 multiple factors. The general response of the storm plasma injection is PSD enhancement through
495 local acceleration. However, this effect is countered by the Dst (SYM-H) effect due to the ring
496 current enhancement, which would cause outward electron drift and a decrease PSD because of
497 the the third adiabatic invariant. This Dst (SYM-H) effect is stronger with increasing L* because
498 at |B| decreases with r^3. Moreover, different type storms can affect radiation belt electrons
499 differently. For example, *Turner et al* (2019) reported that full coronal mass ejection (CME)
500 storms cause MeV electron enhancements at L < ~5 while stream interaction region (SIR) storms
501 cause enhancements at L > ~4.5. CME sheaths and CME ejecta can cause depletions throughout
502 the outer radiation belt.

503

504 **4.5 The rankings of solar wind and magnetospheric parameters by the information transfer**
505 **to the radiation belt electrons**

506 In the previous sections, we calculate the dependence of the PSD on V_{sw}, n_{sw}, P_{dyn}, AL, and
507 SYM-H. V_{sw} transfers the most information to the PSD by significantly larger amount than any
508 other solar wind variables. In this section, we calculate the CMI from other solar wind parameters
509 to the PSD, given V_{sw}. Specifically, we calculate CMI($x \rightarrow$ PSD| V_{sw}) where x = IMF |B|, $B_z < 0$,
510 $B_z > 0$, B_y, Esw, and σ(IMF B).

511 Table 1 ranks these parameters based on the information transfer to the radiation belt
512 electron PSD, given V_{sw} for L* = 3 – 6.5. The information transfer is calculated as i_{tr_max} =
513 maximum of (CMI – mean noise). The information transfer from V_{sw} to the PSD is calculated

514 from CMI($V_{sw} \rightarrow$ PSD| n_{sw}). It shows the dominance of V_{sw} in terms of information transfer to the
515 PSD. SYM-H, which is ranked second, transfers only about a quarter as much information to the
516 PSD. In Table 1, if the response lag time has a broad peak, τ is reported as having a range of
517 values. Table 1 shows that the radiation belt electron response lag time to the solar wind and
518 magnetospheric parameters fall into two categories. The electron response with a small τ ($\tau <$ 15
519 hr) is a decrease in PSD (electron loss) while the response at large τ ($\tau >$ 40 hr) is an enhancement
520 in PSD.

521 Zhao et al. (2017) correlated PSD with solar wind (Vsw, nsw, Pdyn) and magnetospheric
522 parameters (SYM-H, AL) and found that AL has the best correlation with PSD with t = 2-5 days
523 for $\mu >$ 700 MeV G^{-1}. However, their study differs from the present study in two key aspects: (1)
524 their study used daily resolution data; (2) more importantly, they did not remove the effect of Vsw
525 from AL, SYM-H, and other parameters. The second point is particularly consequential because
526 AL negatively correlates with V_{sw} (Figure 11c) and some of the good correlation between AL and
527 PSD can be partially attributed to the good correlation between V_{sw} and PSD.

528 Many of the parameters, namely IMF |B|, IMF $B_z < 0$, IMF B_y, n_{sw}, and P_{dyn}, produce dual
529 response modes in the radiation belt electrons. At small τ ($\tau <$ 15 hr), the response is a decrease
530 in PSD or electron loss while at large τ ($\tau >$ 30 hr), the response is an enhancement in PSD. For
531 these parameters, the ranking is based on the mode that has the higher i_{tr_max}. The response to IMF
532 |B| has roughly the same i_{tr_max} at small and large τ, although Table 1 lists the response to the large
533 τ. The response to IMF|B|, IMF $B_z < 0$, and IMF B_y at $\tau <$ 15 hr is electron loss and is mainly due
534 to their correlations with n_{sw}. If the effect of n_{sw} is removed, this peak will diminish or disappear.
535 An example for IMF $B_z > 0$ is illustrated in Figures 4e and 4f.

536 The ranking presented in Table 1 can be useful for modeling radiation belt electrons. The

table may help modelers decide which parameters need to be considered as inputs to their models.

5. Discussion and conclusion

5.1 Untangling the solar wind and magnetospheric drivers

An important factor that is often ignored and underappreciated in many solar wind-magnetosphere interaction studies is that many solar wind parameters positively or negatively correlate with one another, which may introduce complications and ambiguities in the causal-effect interpretation of the data. In the present study, we use conditional mutual information, CMI, to untangle the effects of the solar wind and magnetospheric drivers of the radiation belt electrons PSD having μ = 725–875 MeV G^{-1} and K = 0.09–0.13 R_E $G^{-0.5}$ (average energy ~1.6 MeV).

The radiation belt electron response time lags to V_{sw}, n_{sw}, AL, and SYM-H obtained from correlational analysis differ from those obtained from CMIs that have removed the effect of the V_{sw} or n_{sw} as summarized in Table 2 (from Figures 2, 11, and 13). For the purpose of facilitating a more precise comparison, Table 2 lists only the peak τ even if the peak may be broad whereas Table 1 lists a range of τ, if the peak is broad. The response lag times obtained by CMIs are deemed more accurate because the effect of V_{sw} or n_{sw} has been removed. For example, CMI($n_{sw} \rightarrow$ PSD$|\ V_{sw}$) peaks at t = 7–11 hr whereas corr($n_{sw} \rightarrow$ PSD) has a minimum at τ = 15 hr (*Lyatsky and Khazanov*, 2008a). The smaller τ is deemed a more accurate time scale for magnetopause shadowing, which physically makes sense and and is consistent with observations (e.g., *Turner et al*., 2014a; *Xiang et al*., 2017; 2018; *Turner and Ukhorskiy*, 2020). The shift in the peak CMI depends on the conditional variable z in the CMI($x \rightarrow y| z$). If the (linear and nonlinear) correlation of z with y is smaller than that between x and y, then removing the effect of z would shift the peak to a larger value and vice versa.

560 The response of the radiation belt electrons to n_{sw} has dual mode. At small τ, n_{sw} negatively
561 correlates with the electron PSD with a peak response time at τ = 7–11 hr, which can be attributed
562 to the magnetopause shadowing effect. However, at large τ (τ > 80 hr), n_{sw} positively correlates
563 with the electron PSD as shown in Figures 2e and 3. It is not clear what causes this positive
564 correlation. n_{sw} may be a proxy for another solar wind parameter. n_{sw} negatively correlates with
565 IMF $B_z < 0$, which may be the real driver. However, n_{sw} and IMF $B_z < 0$ may be both proxies for
566 another parameter. For example, an increase in n_{sw} is sometimes accompanied by n_{sw} fluctuations,
567 which can drive ULF waves in the magnetosphere and accelerate electrons (e.g., *Kepko and Viall*,
568 2019, *Ukhorskiy et al*., 2005). Interestingly, the secondary peak in CMI($n_{sw} \rightarrow$ PSD| V_{sw}) at L* =
569 4.5–5.5 (Figures 6d and 6e) is more prominent and significant than its counterpart in CMI($P_{dyn} \rightarrow$
570 PSD| V_{sw}) (Figures 7d and 7e), suggesting that the driver for the secondary peak may be more
571 related to n_{sw} rather than P_{dyn}. Whichever parameter drives the electron acceleration, the result
572 suggests a rather slow process for electron acceleration, τ > 80 hr. This will be investigated in our
573 follow up study.
574
575 **5.2 The radial dependences of the radiation belt electrons**
576 The responses of radiation belt electrons to V_{sw}, n_{sw}, P_{dyn}, AL, and SYM-H have radial
577 dependence. The data coverage for the electrons with μ = 725–875 MeV G^{-1} and K = 0.09–0.13
578 $R_E\ G^{-0.5}$ is poor for L* < 3 and L* > 6.5. Hence, the present study does not consider these L*
579 ranges. The effect of n_{sw} and P_{dyn} on the radiation belt electron PSD appear to be significant only
580 at L* = 4.5–6 and insignificant at L* = 3–4.5. This suggests that the magnetopause shadowing is
581 effective mostly at L* = 4.5–6. At L* = 6–6.5, there is a high variability in PSD and the bin has
582 the fewest number of points (n = 336) and hence the result is deemed unreliable. In contrast, the

583 effect of V_{sw} on the electron PSD appears to be significant at a larger range of L*, L* = 3.5 to 6.5.

584 An increase in n_{sw} or P_{dyn} compresses the magnetosphere leading to the electron loss at
585 high L*, e.g., L* > 7. However, ULF waves generated throughout the magnetosphere due to the
586 compression would redistribute the loss to lower L*. Our result shows that the electron loss can
587 be seen at L* = 4.5–6, consistent with understanding from observations and simulations (*Turner*
588 *et al*. 2012, 2014a; *Xiang et al*. 2017; 2018; *Turner and Ukhorskiy*, 2020). At higher L*, the noise
589 in the CMI($n_{sw} \rightarrow$ PSD| V_{sw}) is higher, which can be attributed to higher variability of the PSD.
590 For example, the PSD initially decreases due to the magnetopause compression and then increase
591 because of the outward diffusion (*Turner et al*., 2012; *Shprits et al*., 2006). Our result differs from
592 Zhao et al. (2017) that found that P_{dyn} negatively correlates with PSD only at a small range of L*
593 band near 6 (see their Figure 4c).

594 The radiation belt electrons also have strong dependences on the internal state of the
595 magnetosphere. In the present study, this is explored and exemplified with AL and SYM-H, which
596 can be used as proxies for magnetospheric state. However, the dependences on AL and SYM-H
597 vary with radial distance or L*. The dependence of the radiation belt electrons on AL is significant
598 at L* = 4–6 while the dependence on SYM-H is significant at L* = 3–6. The response of the
599 radiation belt electrons to AL and SYM-H peak at τ = 40–80 and τ = 20–60 hr, respectively. These
600 lag times are averaged for all L*. AL and SYM-H are proxies for substorms and storms,
601 respectively. Substorm and storm injections can increase the temperature anisotropy in the inner
602 magnetosphere, which are important for local acceleration mechanism discussed in Section 5.3.
603 However, it is not clear why there is a large difference between the response lag times to AL and
604 that to SYM-H. This difference in response lag times are also seen in the corr(AL $\rightarrow$ PSD) and
605 corr(SYM-H $\rightarrow$ PSD) in Zhao et al. (2017), but their peak τ are smaller, which can be attributed,

606 at least partly, to their usage of daily resolution data and their correlations did not remove the effect
607 of V_{sw}.
608
609 **5.3 Implications to electron acceleration mechanism and transport**
610 One of the fundamental questions in radiation belt physics is how the electrons are
611 accelerated to relativistic energies (> 1 MeV). There have been many proposed mechanisms, but
612 most tend to fall into two categories: (1) local acceleration and (2) radial transport (see review in
613 Friedel et al., 2002).
614 In the local acceleration mechanism, substorms or storms transport low energy electrons (a
615 few to tens of keVs) from the plasma sheet into the inner magnetosphere, which are often referred
616 to as the source population (e.g,, *Baker et al*., 1996; *Tang et al.*, 2017a; *Boyd et al*., 2016). The
617 temperature anisotropy in the source population leads to the growth of the VLF whistler mode
618 chorus waves (e.g., *Meredith et al*., 2001; *W. Li et al*., 2009). Substorms and storms also transport
619 high energy electrons (a few tens to hundreds keVs) electrons from the plasma sheet into the inner
620 magnetosphere, which are commonly referred to as seed population. Then, the chorus waves
621 interact with the seed electrons and energize them to relativistic energies (e.g., *Summers et al*.,
622 1998; 2002; *Horne et al*., 2005; *Omura et al*., 2007; Thorne, 2010; Reeves et al., 2013; *W. Li et*
623 *al.*, 2014).
624 In the radial transport acceleration mechanism, electrons at larger L* get accelerated as
625 they move inward to the inner magnetosphere through interactions with ULF waves (e.g., *Baker*
626 *et al*., 1998; *Li and Temerin*, 2001; *Li et al*., 2005; *Ukhorskiy et al*., 2005; *Mathie and Mann*, 2000;
627 *Elkington et al*., 1999; *Kepko and Viall*, 2019). These ULF waves can be associated with high V_{sw}
628 and Kelvin-Helmholtz Instability (KHI) or n_{sw} or P_{dyn} fluctuations (e.g., *Johnson et al*., 2014;

629 *Engebretson et al.*, 1998; *Vennerstrøm*, 1999; *Claudepierre et al*., 2010; *Takahashi and Ukhorskiy*,
630 2007; *Liu et al*., 2010).

631 The result of CMI($V_{sw} \rightarrow$ PSD| n_{sw}) as a function of L* (Figures 9 and 10) can be interpreted
632 in terms of local acceleration mechanism. Figure 10 suggests that the radiation belt electrons at
633 L* = 4.5–5.5 have the shortest response lag time with peak τ = 35–50 hr and the highest
634 significance. The response lag time is larger and broader at higher L*, τ = 45–65 hr (L* = 5.5–6),
635 τ = 40–100 hr (L* = 6–6.5), and at lower L*, τ = 35–55 hr (L* = 4–4.5) and τ = 45–60 hr (L* =
636 3.5–4). This would suggest that local acceleration peaks at L* = 4.5–5.5 and then subsequent
637 outward and inward diffusion spreads enhancements from this L* band. Previous studies also
638 found evidence for local acceleration at this L* band by examining the MeV PSD or electron fluxes
639 as a function of radial distance (*Green and Kivelson*, 2004; *Boyd et al*., 2018; *Tang et al*., 2017a)
640 or microburst MeV electron precipitation (*O'Brien et al*., 2003). At L* = 4–4.5, there is evidence
641 of weak local acceleration. Its i_{tr} starts increasing at about the same time as that for L* = 4.5–5.5,
642 but its significance is lower than that for L* = 4.5–5.5.

643 Our finding differs from previous studies that attributed the good correlation between Vsw
644 and PSD to ULF waves and radial transport (e.g., Rostoker et al., 1998; Elkington et al., 1999;
645 Mathie and Mann, 2000; Zhao et al., 2017).

646 The radial diffusion time scale can be estimated by considering the peak τ of each L* bin
647 in Figure 10. It is found that the outward diffusion from L* = 5 to 6 is about 2 days per.

648 The result of CMI(AL $\rightarrow$ PSD| V_{sw}) can also be interpreted as consistent with local
649 acceleration at L* = 4–5.5 and inward and outward diffusion to lower and higher L*, respectively.
650 This may not be too surprising because the link between V_{sw} and PSD involves substorm injections.

651 However, the radiation belt electron response lag time appears more complicated for

652 CMI(SYM-H → PSD| V_{sw}) (Figure 14). The peak τ is most significant and smallest at L* = 5–5.5
653 suggesting local acceleration peaks at this L* band. There is evidence for inward and outward
654 diffusion from this L* band. However, there is also evidence for local acceleration at smaller L*.
655 The complication may stem from the competing processes that would increase and decrease PSD
656 and electron fluxes. A decrease of SYM-H would indicate increase in the ring current and the
657 intensity of storms. The general response to storm plasma injections would be an increase in
658 whistler mode chorus waves and electron acceleration, leading to an increase in PSD. However,
659 storm would increase the ring current, which would reduce |B|. This would cause outward
660 diffusion and reduction of PSD as the electrons would attempt to conserve the third adiabatic
661 invariant (*Turner et al.*, 2012). This Dst or SYM-H effect would be stronger with increasing radial
662 distance. This could be a contributing factor in the high noise and variability seen in L* = 6-6.5.
663 Studies have shown that the radiation belt electron response at the outermost L* band can
664 sometimes be enhancement, depletion, or no change (*O'Brien et al*., 2001; *Reeves et al*., 2003).
665 These competing processes may contribute to this variability in the radiation belt response. Also,
666 different types of storms would affect different L* differently (*Turner et al*., 2019).
667
668 **5.4 Ranking of the solar wind and magnetospheric drivers**
669 We rank the solar wind and magnetospheric parameters based on the information transfer
670 to the radiation belt electron PSD. This ranking can be useful for modelers who would like to
671 develop models that input solar wind and magnetospheric parameters and predict radiation belt
672 electrons having energies 1–2 MeV. This is shown in Table 1. The table shows that V_{sw} transfers
673 the most information to the radiation belt electrons and hence should be considered an important,
674 if not the most important, input parameter to radiation belt models. However, SYM-H can also be

an important input parameter for models for two reasons: (1) SYM-H transfers the second most information to the radiation belt electrons; and (2) Out of a long list of parameters (V_{sw}, n_{sw}, P_{dyn}, AL, SYM-H), only SYM-H has information the radiation belt electrons at L* = 3–3.5 albeit only a small amount of information. SYM-H can play a crucial role for models that predict the radiation belt electrons at L* = 3–3.5.

Acknowledgments. The solar wind, SYM-H, and AL dataset were obtained from NASA OMNIweb https://omniweb.gsfc.nasa.gov/. All the derived data products in this paper are available upon request by email (simon.wing@jhuapl.edu). All RBSP-ECT data are publicly available at the website http://www.rbsp-ect.lanl.gov. Simon Wing acknowledges support of NASA Van Allen Probe Contract NNN16AA09T and NASA Grants NNX16AQ87G, 80NSSC20K0704, 80NSSC19K0843, 80NSSC19K0822, 80NSSC20K0188, 80NSSC20K1279, and 80NSSC20K1271. Drew Turner is thankful for funding from NASA grants 80NSSC19K0280 and 80NSSC18K1377. This work has benefitted from discussions within the International Space Science Institute (ISSI) Team # 455 "Complex Systems Perspectives Pertaining to the Research of the Near-Earth Electromagnetic Environment."

694

695 ## References

696 Allison, H.J., Shprits, Y. Y. (2020), Local heating of radiation belt electrons to ultra-relativistic
697 energies. *Nat Commun* **11,** 4533, https://doi.org/10.1038/s41467-020-18053-z

698 Alves, L.R., Souza, V.M., Jauer, P.R. *et al.* The Role of Solar Wind Structures in the Generation
699 of ULF Waves in the Inner Magnetosphere. *Sol Phys* **292,** 92 (2017).
700 https://doi.org/10.1007/s11207-017-1113-4

701 Baker, D. N., R. L. McPherron, T. E. Cayton, and R. W. Klebesadel (1990), Linear prediction
702 filter analysis of relativistic electron properties at 6.6 R_E , J. Geophys. Res., 95(A9),15133–
703 15140, doi:10.1029/JA095iA09p15133.

704 Baker, D. N., Pulkkinen, T. I., Angelopoulos, V., Baumjohann, W., and McPherron, R.
705 L. (1996), Neutral line model of substorms: Past results and present view, *J. Geophys.*
706 *Res.*, 101(A6), 12975– 13010, doi:10.1029/95JA03753.

707 Baker, D. N., X Li, J. B Blake, S. Kanekal (1998), Strong electron acceleration in the Earth's
708 magnetosphere, Adv. Space Res., 21, 609-613, doi:10.1016/S0273-1177(97)00970-8.

709 Baker, D. N., et al. (2012), The Relativistic Electron-Proton Telescope (REPT) Instrument on
710 Board the Radiation Belt Storm Probes (RBSP) Spacecraft: Characterization of Earth's
711 Radiation Belt High-Energy Particle Populations, Space Sci. Rev., doi:10.1007/s11214-012-
712 9950-9.

713 Baker, D.N., Erickson, P.J., Fennell, J.F. *et al.* Space Weather Effects in the Earth's Radiation
714 Belts. *Space Sci Rev* **214,** 17 (2018). https://doi.org/10.1007/s11214-017-0452-7

715 Baker, D. N., Hoxie, V., Zhao, H., Jaynes, A. N., Kanekal, S., Li, X., & Elkington,
716 S. (2019a). Multiyear measurements of radiation belt electrons: Acceleration, transport, and

loss. *Journal of Geophysical Research: Space Physics*, 124, 2588– 2602. https://doi.org/10.1029/2018JA026259

Baker, D. N., Zhao, H., Li, X., Kanekal, S. G., Jaynes, A. N., Kress, B. T., et al. (2019b). Comparison of Van Allen Probes Energetic Electron Data with corresponding GOES-15 Measurements: 2012–2018. Journal of Geophysical Research: Space Physics,124, https://doi.org/10.1029/2019JA027331

Balasis, G., Daglis, I. A., Papadimitriou, C., Kalimeri, M., Anastasiadis, A., and Eftaxias, K. (2008), Dynamical complexity in D_{st} time series using non-extensive Tsallis entropy, *Geophys. Res. Lett.*, 35, L14102, doi:10.1029/2008GL034743.

Balasis, G., Daglis, I. A., Papadimitriou, C., Kalimeri, M., Anastasiadis, A., and Eftaxias, K. (2009), Investigating dynamical complexity in the magnetosphere using various entropy measures, *J. Geophys. Res.*, 114, A00D06, doi:10.1029/2008JA014035.

Balasis, G., C. Papadimitriou, I. A. Daglis, A. Anastasiadis, L. Athanasopoulou, andK. Eftaxias (2011), Signatures of discrete scale invariance in D_{st} time series, *Geophys. Res. Lett.*, 38, L13103, doi: 10.1029/2011GL048019.

Balasis, G.; Donner, R.V.; Potirakis, S.M.; Runge, J.; Papadimitriou, C.; Daglis, I.A.; Eftaxias, K.; Kurths (2013), J. Statistical mechanics and information-theoretic perspectives on complexity in the Earth system. Entropy, 15, 4844–4888, doi:10.3390/e15114844.

Balikhin, M. A., R. J. Boynton, S. A. Billings, M. Gedalin, N. Ganushkina, D. Coca, and H. Wei (2010), Data based quest for solar wind-magnetosphere coupling function, Geophys. Res. Lett., 37, L24107, doi:10.1029/2010GL045733.

738 Balikhin, M. A., R. J. Boynton, S. N. Walker, J. E. Borovsky, S. A. Billings, and H. L.
739 Wei(2011), Using the NARMAX approach to model the evolution of energetic electrons
740 fluxes at geostationary orbit, Geophys. Res. Lett., 38, L18105, doi:10.1029/2011GL048980.
741 Birn, J., and E. W. Hones Jr. (1981), Three-dimensional computer modeling of dynamic
742 reconnection in the geomagnetic tail, J. Geophys. Res., 86, 6802–6808,
743 doi:10.1029/JA086iA08p06802.
744 Birn, J., M. F. Thomsen, J. E. Borovsky, G. D. Reeves, D. J. McComas, and R. D. Belian (1997),
745 Characteristic plasma properties during disper- sionless substorm injections at
746 geosynchronous orbit, J. Geophys. Res., 102, 2309–2324.
747 Birn, J., M. Hesse, and K. Schindler, Entropy conservation in simulations of magnetic
748 reconnection (2006b), Phys. Of Plasma, 13, 092117, doi: 10.1063/1.2349440.
749 Blake, J.B., Carranza, P.A., Claudepierre, S.G. *et al.* The *Magnetic Electron Ion*
750 *Spectrometer* (MagEIS) Instruments Aboard the Radiation Belt Storm Probes (RBSP)
751 Spacecraft. *Space Sci Rev* **179,** 383–421 (2013). https://doi.org/10.1007/s11214-013-9991-
752 8
753 Borovsky, J. E. (2012), The velocity and magnetic field fluctuations of the solar wind at 1 AU:
754 Statistical analysis of Fourier spectra and correlations with plasma properties, *J. Geophys.*
755 *Res.*, 117, A05104, doi:10.1029/2011JA017499.
756 Borovsky, J. E., and Denton, M. H. (2014), Exploring the cross correlations and autocorrelations
757 of the ULF indices and incorporating the ULF indices into the systems science of the solar
758 wind-driven magnetosphere, *J. Geophys. Res. Space Physics*, 119, 4307– 4334,
759 doi:10.1002/2014JA019876.

Borovsky, J. E. (2016), The plasma structure of coronal hole solar wind: Origins and evolution, *J. Geophys. Res. Space Physics*, 121, 5055– 5087, doi:10.1002/2016JA022686.

Borovsky, J. E. (2017). Time-integral correlations of multiple variables with the relativistic-electron flux at geosynchronous orbit: The strong roles of substorm-injected electrons and the ion plasma sheet. *Journal of Geophysical Research: Space Physics*, 122, 11,961– 11,990. https://doi.org/10.1002/2017JA024476

Borovsky, J. E. (2018), On the origins of the intercorrelations between solar wind variables. *Journal of Geophysical Research: Space Physics*, 123, 20– 29. https://doi.org/10.1002/2017JA024650

Borovsky, J. E. (2020), What magnetospheric and ionospheric researchers should know about the solar wind, *J. Atmos. Sol. Phys*., 204, 105271, https://doi.org/10.1016/j.jastp.2020.105271.

Boyd, A. J., Spence, H. E., Claudepierre, S. G., Fennell, J. F., Blake, J. B., Baker, D. N., Reeves, G. D., and Turner, D. L. (2014), Quantifying the radiation belt seed population in the March 17, 2013 electron acceleration event, *Geophys. Res. Lett.*, 41, 2275– 2281, doi:10.1002/2014GL059626.

Boyd, A. J., Spence, H. E., Huang, C.-L., Reeves, G. D., Baker, D. N., Turner, D. L., Claudepierre, S. G., Fennell, J. F., Blake, J. B., and Shprits, Y. Y. (2016), Statistical properties of the radiation belt seed population, *J. Geophys. Res. Space Physics*, 121, 7636– 7646, doi:10.1002/2016JA022652.

Boyd, A. J., Turner, D. L., Reeves, G. D., Spence, H. E., Baker, D. N., & Blake, J. B. (2018). What causes radiation belt enhancements: A survey of the Van Allen Probes Era. *Geophysical Research Letters*, 45, 5253– 5259. https://doi.org/10.1029/2018GL077699

Boyd, A. J., Spence, H. E., Reeves, G. D., Funsten, H. O., Skoug, R. M., Larsen, B. A., et al. (2021). RBSP-ECT combined pitch angle resolved electron flux data product. *Journal of Geophysical Research: Space Physics*, 126, e2020JA028637. https://doi.org/10.1029/2020JA028637

Claudepierre, S. G., M. K. Hudson, W. Lotko, J. G. Lyon, and R. E. Denton (2010), Solar wind driving of magnetospheric ULF waves: Field line resonances driven by dynamic pressure fluctuations, J. Geophys. Res., 115, A11202, doi:10.1029/2010JA015399.

Consolini, G., R. Tozzi, and P. De Michelis (2009), Complexity in the sunspot cycle, A&A 506, 1381–1391, DOI: 10.1051/0004-6361/200811074

Davis, T. N., and Sugiura, M. (1966), Auroral electrojet activity index *AE* and its universal time variations, *J. Geophys. Res.*, 71(3), 785– 801, doi:10.1029/JZ071i003p00785.

Darbellay, G. A., and I. Vajda (1999), Estimation of the Information by an Adaptive Partitioning of the Observations Space, IEEE Transactions on Information Theory, 45, 1315–1321.

De Michelis, P., G. Consolini, M. Materassi, and R. Tozzi (2011), An information theory approach to the storm-substorm relationship, J. Geophys. Res., 116, A08225, doi:10.1029/2011JA016535.

De Michelis, P.; Tozzi, R.; Consolini, G. (2017), Statistical analysis of geomagnetic field intensity differences between ASM and VFM instruments onboard Swarm constellation. Earth Planets Space, 69, 24, doi:10.1186/s40623-016-0583-1.

Dessler, A., and E. Parker (1959), Hydromagnetic theory of geomagnetic storms, *J. Geophys. Res.*, **64**(12), 2239–2252, doi:10.1029/JZ064i012p02239.

803 Elkington, S. R., M. K. Hudson, and A. A. Chan (1999), Acceleration of relativistic electrons via
804 drift-resonant interaction with toroidal-mode Pc-5 ULF oscillations, Geophys. Res. Lett., 26,
805 3273.
806 Elkington, S. R., Hudson, M. K., and Chan, A. A. (2003), Resonant acceleration and diffusion of
807 outer zone electrons in an asymmetric geomagnetic field, *J. Geophys. Res.*, 108, 1116,
808 doi:10.1029/2001JA009202
809 Engebretson, M., K.-H. Glassmeier, M. Stellmacher, W. J. Hughes, and H. Lühr (1998), The
810 dependence of high-latitude PcS wave power on solar wind velocity and on the phase of
811 high-speed solar wind streams, J. Geophys. Res., 103(A11), 26271–26283,
812 doi:10.1029/97JA03143.
813 Friedel, R. H. W., G. D. Reeves, and T. Obara (2002), Relativistic electron dy- namics in the inner
814 magnetosphere—A review, J. Atmos. Sol. Terr. Phys., 64, 265.
815 Green, J. C., and M. G. Kivelson (2004), Relativistic electrons in the outer radiation belt:
816 Differentiating between acceleration mechanisms, J. Geophys. Res., 109, A03213,
817 doi:10.1029/2003JA010153.
818 Horne, R. B., R. M. Thorne, S. A. Glauert, J. M. Albert, N. P. Meredith, and R. R. Anderson
819 (2005), Timescale for radiation belt electron acceleration by whistler mode chorus waves,J.
820 Geophys. Res., 110, A03225, doi:10.1029/2004JA010811
821 Hudson, M. K., Kress, B. T., Mueller, H.-R., Zastrow, J. A., & Blake, J. B. (2008). Relationship
822 of the Van Allen radiation belts to solar wind drivers. Journal of Atmospheric and Solar-
823 Terrestrial Physics, 70, 708–729. https://doi.org/10.1016/j.jastp.2007.11.003

824 Hundhausen, A. J., S. J. Bame, J. R. Asbridge, and S. J. Sydoriak (1970), Solar wind proton
825 properties: Vela 3 observations from July 1965 to June 1967, J. Geophys.
826 Res., 75(25),4643–4657, doi:10.1029/JA075i025p04643
827 Iles, R. H. A., Meredith, N. P., Fazakerley, A. N., and Horne, R. B. (2006), Phase space density
828 analysis of the outer radiation belt energetic electron dynamics, *J. Geophys. Res.*, 111,
829 A03204, doi:10.1029/2005JA011206.
830 Iyemori, T. (1990), Storm-time magnetospheric currents inferred from mid-latitude geomagnetic
831 field variations, J. Geomag. Geoelectr., 42, 1249–1265.
832 Jaynes, A. N., et al. (2015), Source and seed populations for relativistic electrons: Their roles in
833 radiation belt changes, J. Geophys. Res. Space Physics,120, doi:10.1002/2015JA021234.
834 Jaynes, A. N., Ali, A. F., Elkington, S. R., Malaspina, D. M., Baker, D. N., Li, X., et al.
835 (2018). Fast diffusion of ultrarelativistic electrons in the outer radiation belt: 17 March 2015
836 storm event. *Geophysical Research Letters*, 45, 10,874– 10,882.
837 https://doi.org/10.1029/2018GL079786
838 Johnson, J. R., and S. Wing (2005), A solar cycle dependence of nonlinearity in magnetospheric
839 activity, J. Geophys. Res., 110, A04211, doi:10.1029/2004JA010638.
840 Johnson, J. R., and S. Wing (2014), External versus internal triggering of substorms: An
841 information-theoretical approach, Geophys. Res. Lett., 41, 5748–5754,
842 doi:10.1002/2014GL060928.
843 Johnson, J. R., S. Wing, and P. A. Delamere (2014), Kelvin Helmholtz Instability in Planetary
844 Magnetospheres, Space Sci. Rev., 184, 1 – 31, doi:10.1007/s11214-014-0085-z.

Johnson, J. R., Wing, S., and Camporeale, E. (2018), Transfer entropy and cumulant-based cost as measures of nonlinear causal relationships in space plasmas: applications to D_{st}, Ann. Geophys., 36, 945-952, https://doi.org/10.5194/angeo-36-945-2018

Katus, R. M., Liemohn, M. W., Gallagher, D. L., Ridley, A., and Zou, S. (2013), Evidence for potential and inductive convection during intense geomagnetic events using normalized superposed epoch analysis, *J. Geophys. Res. Space Physics*, 118, 181– 191, doi:10.1029/2012JA017915.

Kellerman, A. C., and Y. Y. Shprits (2012), On the influence of solar wind conditions on the outer-electron radiation belt, J. Geophys. Res., 117, A05217, doi:10.1029/2011JA017253.

Kepko, L., & Viall, N. M. (2019). The source, significance, and magnetospheric impact of periodic density structures within stream interaction regions. Journal of Geophysical Research: Space Physics, 124, 7722– 7743. https://doi.org/10.1029/2019JA026962

Lejosne, S., Kollmann, P. Radiation Belt Radial Diffusion at Earth and Beyond. *Space Sci Rev* **216,** 19 (2020). https://doi.org/10.1007/s11214-020-0642-6

Li, W. (1990), Mutual Information Functions Versus Correlation Functions, J. Stat. Phys., 60, 823–837.

Li, W., Thorne, R. M., Angelopoulos, V., Bonnell, J. W., McFadden, J. P., Carlson, C. W., LeContel, O., Roux, A., Glassmeier, K. H., and Auster, H. U. (2009), Evaluation of whistler-mode chorus intensification on the nightside during an injection event observed on the THEMIS spacecraft, *J. Geophys. Res.*, 114, A00C14, doi:10.1029/2008JA013554.

Li, W., et al. (2014), Radiation belt electron acceleration by chorus waves during the 17 March 2013 storm, *J. Geophys. Res. Space Physics*, 119, 4681– 4693, doi:10.1002/2014JA019945.

Li, X., and M. A. Temerin (2001), The electron radiation belt, Space Sci. Rev., 95, 569 - 580.

Li, X., M. Temerin, D. Baker, G. Reeves, and D. Larson (2001), Quantitative prediction of radiation belt electrons at geostationary orbit based on solar wind measurements,*Geophys. Res. Lett.*, **28**(9), 1887–1890.

Li, X., D. N. Baker, M. Temerin, G. Reeves, R. Friedel, and C. Shen (2005), Energetic electrons, 50 keV to 6 MeV, at geosynchronous orbit: Their responses to solar wind variations, Space Weather, 3, S04001, doi:10.1029/2004SW000105.

Li, X., Barker, A. B., Baker, D. N., Tu, W. C., Sarris, T. E., Selesnick, R. S., Friedel, R., and Shen, C. (2009), Modeling the deep penetration of outer belt electrons during the "Halloween" magnetic storm in 2003, *Space Weather*, 7, S02004, doi:10.1029/2008SW000418.

Liu, W., Sarris, T. E., Li, X., Ergun, R., Angelopoulos, V., Bonnell, J., and Glassmeier, K. H. (2010), Solar wind influence on Pc4 and Pc5 ULF wave activity in the inner magnetosphere, *J. Geophys. Res.*, 115, A12201, doi:10.1029/2010JA015299.

Lui, A. T. Y. (1991), Extended consideration of a synthesis model for magnetospheric substorms, in Magnetospheric Substorms, pp. 43-60, Geophys. Monog., 64, edited by J. R. Kan, T. A. Potemra, S. Kokubun, and T. Ijima, AGU, Washington D.C.,

Lyatsky, W., and G. V. Khazanov (2008a), Effect of solar wind density on relativistic electrons at geosynchronous orbit, Geophys. Res. Lett., 35, L03109, doi:10.1029/2007GL032524.

Lyatsky, W., and G. V. Khazanov (2008b), Effect of geomagnetic disturbances and solar wind density on relativistic electrons at geostationary orbit, J. Geophys. Res., 113, A08224, doi:10.1029/2008JA013048.

Lyons, L. R. (1995), A new theory for magnetospheric substorms, J. Geophys. Res., 100, 19,069–19,082, doi:10.1029/95JA01344.

890 Lyons, L. R., G. T. Blanchard, J. C. Samson, R. P. Lepping, T. Yamamoto, and T. Moretto (1997),
891 Coordinated observations demonstrating external substorm triggering, J. Geophys. Res.,
892 102, 27,039–27,052, doi:10.1029/97JA02639.
893 Maggiolo, R., Hamrin, M., De Keyser, J., Pitkänen, T., Cessateur, G., Gunell, H., & Maes, L.
894 (2017). The delayed time response of geomagnetic activity to the solar wind. Journal of
895 Geophysical Research: Space Physics, 122, 11,109– 11,127.
896 https://doi.org/10.1002/2016JA023793
897 Mann, I. R., Ozeke, L. G., Murphy, K. R., Claudepierre, S. G., Turner, D. L., Baker, D. N., et al.
898 (2016). Explaining the dynamics of the ultra- relativistic third Van Allen Radiation belt.
899 Nature Physics, 12(10), 978–983. https://doi.org/10.1038/NPHYS3799
900 March, T. K., Chapman, S. C., and Dendy, R. O. (2005), Mutual information between
901 geomagnetic indices and the solar wind as seen by WIND: Implications for propagation time
902 estimates, *Geophys. Res. Lett.*, 32, L04101, doi:10.1029/2004GL021677.
903 Mathie, R. A., & Mann, I. R. (2000). A correlation between extended intervals of ULF wave power
904 and stormtime geosynchronous relativistic electron flux enhancements. Geophysical
905 Research Letters, 27(20), 3261–3264. https://doi.org/10.1029/2000gl003822
906 McPherron, R. (1991), Physical processes producing magnetospheric substorms and magnetic
907 storms, in Geomagnetism, edited by J. Jacobs, pp. 593–739, Academic Press, London, U. K.
908 McPherron, R. L., T. Terasawa, and A. Nishida (1986), Solar wind triggering of substorm
909 expansion onset, J. Geomagn. Geoelectr., 38(11), 1089–1108, doi:10.5636/jgg.38.1089.
910 Manshour,P., Balasis,G.; Consolini, G.; Papadimitriou, C., Paluš, M. (2021), Causality and
911 Information Transfer Between the Solar Wind and the Magnetosphere–Ionosphere System.
912 *Entropy*, *23*, 390. https://doi.org/10.3390/e23040390

913 Materassi, M., L. Ciraolo, G. Consolini, and N. Smith (2011), Predictive Space Weather: An
914 information theory approach, Adv. Space Res., 47, 877–885, doi:10/106/j.asr.2010.10.026.
915 Mathie, R. A., and I. R. Mann (2000), A correlation between extended intervals of ULF wave
916 power and storm-time geosynchronous relativistic electron flux enhancements, *Geophys.*
917 *Res. Lett.*, **27**, 3621–3264, doi:10.1029/2000GL003822.
918 Mathie, R. A., and I. R. Mann (2001), On the solar wind control of Pc5 ULF pulsation power at
919 mid-latitudes: Implications for MeV electron acceleration in the outer radiation belt, J.
920 Geophys. Res., 106(A12), 29783–29796, doi:10.1029/2001JA000002.
921 Mauk, B. H., N. J. Fox, S. G. Kanekal, R. L. Kessel, D. G. Sibeck, and A. Ukhorskiy (2013),
922 Science objectives and rationale for the radiation belt storm probes mission, Space Science
923 Review, *179*(1-4), 3–27, doi:10.1007/s11214-012-9908-y.
924 Meredith, N. P., Horne, R. B., and Anderson, R. R. (2001), Substorm dependence of chorus
925 amplitudes: Implications for the acceleration of electrons to relativistic energies, *J. Geophys.*
926 *Res.*, 106(A7), 13165– 13178, doi:10.1029/2000JA900156.
927 Miyoshi, Y., R. Kataoka, Y. Kasahara, A. Kumamoto, T. Nagai, and M. F. Thomsen (2013), High-
928 speed solar wind with southward interplanetary magnetic field causes relativistic electron
929 flux enhancement of the outer radiation belt via enhanced condition of whistler waves,
930 Geophys. Res. Lett., 40, doi:10.1002/grl.50916.
931 Newell, P. T., K. Liou, J.W. Gjerloev, T. Sotirelis, S. Wing, E.J. Mitchell (2016), Substorm
932 probabilities are best predicted from solar wind speed, J. Atmos. Sol. Terr. Phys., 146, 28-
933 37, doi:10.1016/j.jastp.2016.04.019.

O'Brien, T. P., McPherron, R. L., Sornette, D., Reeves, G. D., Friedel, R., and Singer, H. J. (2001), Which magnetic storms produce relativistic electrons at geosynchronous orbit?, *J. Geophys. Res.*, 106(A8), 15533– 15544, doi:10.1029/2001JA000052.

O'Brien, T. P., Lorentzen, K. R., Mann, I. R., Meredith, N. P., Blake, J. B., Fennell, J. F., Looper, M. D., Milling, D. K., and Anderson, R. R. (2003), Energization of relativistic electrons in the presence of ULF power and MeV microbursts: Evidence for dual ULF and VLF acceleration, J. Geophys. Res., 108, 1329, doi:10.1029/2002JA009784, A8.

Onsager, T. G., J. C. Green, G. D. Reeves, and H. J. Singer (2007), Solar wind and magnetospheric conditions leading to the abrupt loss of outer radiation belt electrons, J. Geophys. Res., 112, A01202, doi:10.1029/2006JA011708.

Omura, Y., N. Furuya, and D. Summers (2007), Relativistic turning acceleration of resonant electrons by coherent whistler mode waves in a dipole magnetic field, J. Geophys. Res., 112, A06236, doi:10.1029/2006JA012243

Papadimitriou, Constantinos; Balasis, Georgios; Boutsi, Adamantia Z.; Daglis, Ioannis A.; Giannakis, Omiros; Anastasiadis, Anastasios; Michelis, Paola D.; Consolini, Giuseppe. (2020), Dynamical Complexity of the 2015 St. Patrick's Day Magnetic Storm at Swarm Altitudes Using Entropy Measures, *Entropy*, 22, 5, 574, https://doi.org/10.3390/e22050574

Paulikas, G. A., and J. B. Blake (1979), Effects of the solar wind on magnetospheric dynamics: Energetic electrons at the synchronous orbit, in *Quantitative Modeling of Magnetospheric Processes*, *Geophys. Monogr. Ser.*, Vol 21, pp. 180-202, AGU, Washington D.C.

Pinto, V. A., Kim, H.-J., Lyons, L. R., & Bortnik, J. (2018). Interplanetary parameters leading to relativistic electron enhancement and persistent depletion events at geosynchronous orbit

and potential for prediction. *Journal of Geophysical Research: Space Physics*, 123, 1134– 1145. https://doi.org/10.1002/2017JA024902

Prichard, D., and J. Theiler (1995), Generalized redundancies for time series analysis, *Physica D: Non-linear Phenomena,* 84, 476–493, doi:10.1016/0167-2789(95)00041-2.

Reeves, G. D. (1998), Relativistic electrons and magnetic storms: 1992–1995, Geophys. Res. Lett., 25, 1817–1820, doi:10.1029/98GL01398.

Reeves, G. D., McAdams, K. L., Friedel, R. H. W., and O'Brien, T. P. (2003), Acceleration and loss of relativistic electrons during geomagnetic storms, *Geophys. Res. Lett.*, 30, 1529, doi:10.1029/2002GL016513

Reeves, G. D. (2007), Radiation Belt Storm Probes: A New Mission for Space Weather Forecasting. Space Weather, 5: n/a. doi:10.1029/2007SW000341

Reeves, G. D., S. K. Morley, R. H. W. Friedel, M. G. Henderson, T. E. Cayton, G. Cunningham, J. B. Blake, R. A. Christensen, and D. Thomsen (2011), On the relationship between relativistic electron flux and solar wind velocity: Paulikas and Blake revisited, J. Geophys. Res., 116, A02213, doi:10.1029/2010JA015735.

Reeves, G., S. Morley, and G. Cunningham (2013), Long-term variations in solar wind velocity and radiation belt electrons, J. Geophys. Res. Space Physics, 118, 1040–1048, doi:10.1002/jgra.50126.

Rigler, E. J., M. Wiltberger, and D. N. Baker (2007), Radiation belt electrons respond to multiple solar wind inputs, J. Geophys. Res., 112, A06208, doi:10.1029/2006JA012181

Roederer, J. G. (1970), Dynamics of Geomagnetically Trapped Radiation, Springer, New York, https://doi.org/ 10.1007/978-3-642-49300-3

Rostoker, G. (1983), Triggering of expansive phase intensifications of magnetospheric substorms

by northward turnings of the interplanetary magnetic field, J. Geophys. Res., 88, 6981–6993, doi:10.1029/JA088iA09p06981.

Rostoker, G., S. Skone, and D. N. Baker (1998), On the origin of relativistic electrons in the magnetosphere associated with some geomagnetic storms,*Geophys. Res. Lett.*, **25**, 3701–3704, doi:10.1029/98GL02801.

Runge, J., Balasis, G., Daglis, I.A. *et al.* Common solar wind drivers behind magnetic storm–magnetospheric substorm dependency. *Sci Rep* **8,** 16987 (2018). https://doi.org/10.1038/s41598-018-35250-5

Schulz, M., and L.J. Lanzerotti (1974) , Particle Diffusion in the Radiation Belts, Springer, Berlin, 1974, https:// doi.org/10.1007/978-3-642-65675-0

Simms, L. E., V. Pilipenko, M. J. Engebretson, G. D. Reeves, A. J. Smith, and M. Clilverd (2014),Prediction of relativistic electron flux at geostationary orbit following storms: Multiple regression analysis, J. Geophys. Res. Space Physics, 119, 7297–7318, doi:10.1002/2014JA019955.

Shprits, Y. Y., R. M. Thorne, R. Friedel, G. D. Reeves, J. Fennell, D. N. Baker, and S. G. Kanekal (2006), Outward radial diffusion driven by losses at magnetopause, J. Geophys. Res., 111, A11214, doi:10.1029/2006JA011657

Shprits, Y. Y., D. A. Subbotin, N. P. Meredith, S. R. Elkington (2008), Review of modeling of losses and sources of relativistic electrons in the outer radiation belt II: Local acceleration and loss, J. Atmos. Sol. Terr. Phys., 70, 1694-1713, doi:10.1016/j.jastp.2008.06.014.

Shprits, Y. Y., D. Subbotin, and B. Ni (2009), Evolution of electron fluxes in the outer radiation belt computed with the VERB code, J. Geophys. Res., 114, A11209, doi:10.1029/2008JA013784.

Smirnov, A. G., Berrendorf, M., Shprits, Y. Y., Kronberg, E. A., Allison, H. J., Aseev, N. A., et al. (2020). Medium energy electron flux in earth's outer radiation belt (MERLIN): A machine learning model. *Space Weather*, 18, e2020SW002532. https://doi.org/10.1029/2020SW002532

Snelling, Jesse M., Jay R. Johnson, Jake Willard, Yosia Nurhan, Jonathan Homan, and Simon Wing (2020), Information Theoretical Approach to Understanding Flare Waiting Times, The Astrophysical Journal, 899, 148, http://dx.doi.org/10.3847/1538-4357/aba7b9

Spence, H.E., Reeves, G.D., Baker, D.N. et al. (2013), Science Goals and Overview of the Radiation Belt Storm Probes (RBSP) Energetic Particle, Composition, and Thermal Plasma (ECT) Suite on NASA's Van Allen Probes Mission. Space Sci Rev 179, 311–336, https://doi.org/10.1007/s11214-013-0007-5

Stumpo, Mirko; Consolini, Giuseppe; Alberti, Tommaso; Quattrociocchi, Virgilio. 2020. "Measuring Information Coupling between the Solar Wind and the Magnetosphere–Ionosphere System" *Entropy* 22, no. 3: 276. https://doi.org/10.3390/e22030276

Summers, D., R. M. Thorne, and F. Xiao (1998), Relativistic theory of wave-particle resonant diffusion with application to electron acceleration in the magnetosphere, J. Geophys. Res., 103(A9), 20487–20500, doi:10.1029/98JA01740.

Summers, D., Ma, C., Meredith, N. P., Horne, R. B., Thorne, R. M., Heynderickx, D., and Anderson, R. R. (2002), Model of the energization of outer-zone electrons by whistler-mode chorus during the October 9, 1990 geomagnetic storm, *Geophys. Res. Lett.*, 29(24), 2174, doi:10.1029/2002GL016039.

Summers, D., B. Ni, and N. P. Meredith (2007), Timescales for radiation belt electron acceleration and loss due to resonant wave-particle interactions: 1. Theory, J. Geophys. Res., 112, A04206, doi:10.1029/2006JA011801.

Tang, C. L., Wang, Y. X., Ni, B., Zhang, J.-C., Reeves, G. D., Su, Z. P., Baker, D. N., Spence, H. E., Funsten, H. O., and Blake, J. B. (2017a), Radiation belt seed population and its association with the relativistic electron dynamics: A statistical study, *J. Geophys. Res. Space Physics*, 122, 5261– 5276, doi:10.1002/2017JA023905.

Tang, C. L., Wang, Y. X., Ni, B., Su, Z. P., Reeves, G. D., Zhang, J.-C., Baker, D. N., Spence, H. E., Funsten, H. O., and Blake, J. B. (2017b), The effects of magnetospheric processes on

relativistic electron dynamics in the Earth's outer radiation belt, *J. Geophys. Res. Space Physics*, 122, 9952– 9968, doi:10.1002/2017JA024407.

Takahashi, K., and Ukhorskiy, A. Y. (2007), Solar wind control of Pc5 pulsation power at geosynchronous orbit, *J. Geophys. Res.*, 112, A11205, doi:10.1029/2007JA012483.

Thorne, R. M. (2010), Radiation belt dynamics: The importance of wave-particle interactions,Geophys. Res. Lett., 37, L22107, doi:10.1029/2010GL044990

Thorne, R. M., et al. (2013), Rapid local acceleration of relativistic radiation-belt electrons by magnetospheric chorus, Nature, 504(7480), 411–414, doi:10.1038/nature12889.

Tsonis, A. A. (2001), Probing the linearity and nonlinearity in the transitions of the atmospheric circulation, Nonlinear Processes in Geophysics, 8, 341–345.

Turner, D. L., and Li, X. (2008), Quantitative forecast of relativistic electron flux at geosynchronous orbit based on low-energy electron flux, Space Weather, 6, S05005, doi:10.1029/2007SW000354.

Turner, D. L., and X. Li (2011), Using spacecraft measurements ahead of Earth in the Parker spiral to improve terrestrial space weather forecasts, Space Weather, 9, S01002, doi:10.1029/2010SW000627

Turner, D. L., Y. Shprits, M. Hartinger, and V. Angelopoulos (2012), Explaining sudden losses of outer radiation belt electrons during geomagnetic storms, Nat. Phys., 8, 208–212, doi:10.1038/nphys2185.

Turner, D. L., et al. (2014a), On the cause and extent of outer radiation belt losses during the 30 September 2012 dropout event, *J. Geophys. Res. Space Physics*, 119, 1530– 1540, doi:10.1002/2013JA019446.

Turner, D. L., et al. (2014b), Competing source and loss mechanisms due to wave-particle interactions in Earth's outer radiation belt during the 30 September to 3 October 2012 geomagnetic storm, *J. Geophys. Res. Space Physics*, 119, 1960– 1979, doi:10.1002/2014JA019770.

1058 Turner, D. L., Kilpua, E. K. J., Hietala, H., Claudepierre, S. G., O'Brien, T. P., Fennell, J. F., et al.
1059 (2019). The response of Earth's electron radiation belts to geomagnetic storms: Statistics
1060 from the Van Allen Probes era including effects from different storm drivers. Journal of
1061 Geophysical Research: Space Physics, 124, 1013– 1034.
1062 https://doi.org/10.1029/2018JA026066
1063 Turner, D. L., and A. Y. Ukhorskiy (2020), Chapter 1 - Outer radiation belt losses by
1064 magnetopause incursions and outward radial transport: new insight and outstanding
1065 questions from the Van Allen Probes era**,** in The dynamic loss of Earth's radiation belts eds.
1066 Allison N. Jaynes and Maria E. Usanova, Elsevier (2020), pp. 1–20, ISBN 9780128133712,
1067 https://doi.org/10.1016/B978-0-12-813371-2.00001-9
1068 Ukhorskiy, A. Y., M. I. Sitnov, A. S. Sharma, B. J. Anderson, S. Ohtani, and A. T. Y. Lui (2004),
1069 Data-derived forecasting model for relativistic electron intensity at geosynchronous
1070 orbit,Geophys. Res. Lett., 31, L09806, doi:10.1029/2004GL019616.
1071 Ukhorskiy, A. Y., K. Takahashi, B. J. Anderson, and H. Korth (2005), Impact of toroidal ULF
1072 waves on the outer radiation belt electrons, J. Geophys. Res., 110, A10202,
1073 doi:10.1029/2005JA011017.
1074 Ukhorskiy, A. Y., B. J. Anderson, P. C. Brandt, and N. A. Tsyganenko (2006), Storm time
1075 evolution of the outer radiation belt: Transport and losses, J. Geophys. Res., 111, A11S03,
1076 doi:10.1029/2006JA011690.
1077 Vassiliadis, D., S. F. Fung, and A. J. Klimas (2005), Solar, interplanetary, and magnetospheric
1078 parameters for the radiation belt energetic electron flux, J. Geophys. Res., 110, A04201,
1079 doi:10.1029/2004JA010443.
1080 Vennerstrøm, S. (1999), Dayside magnetic ULF power at high latitudes: A possible long-term

proxy for the solar wind velocity?, J. Geophys. Res., 104(A5), 10145–10157, doi:10.1029/1999JA900015.

Wing, S., Johnson, J. R., Jen, J., Meng, C.-I., Sibeck, D. G., Bechtold, K., Freeman, J., Costello, K., Balikhin, M., and Takahashi, K. (2005), Kp forecast models, *J. Geophys. Res.*, 110, A04203, doi:10.1029/2004JA010500.

Wing, S., J. R. Johnson, C. C. Chaston, M. Echim, C. P. Escoubet, B. Lavraud, C. Lemon, K. Nykyri, A. Otto, J. Raeder, and C.-P. Wang (2014), Review of solar wind entry into and transport within the plasma sheet, Space Science Reviews, 184, 33 – 86, doi:10.1007/s11214-014-0108-9

Wing, S., J. R. Johnson, E. Camporeale, and G. D. Reeves (2016), Information theoretical approach to discovering solar wind drivers of the outer radiation belt, J. Geophys. Res. Space Physics, 121, 9378–9399, doi:10.1002/2016JA022711

Wing, S., J. Johnson, and A. Vourlidas (2018), Information theoretic approach to discovering causalities in the solar cycle, *Ap J*, **854,** 85, https://doi.org/10.3847/1538-4357/aaa8e7

Wing, S, J. R. Johnson (2019), Applications of Information Theory in Solar and Space Physics, *Entropy*, 21(2):140, https://doi.org/10.3390/e21020140

Wing, S., P. C. Brandt, D. G. Mitchell, J. R. Johnson, W. S. Kurth and J. D. Menietti (2020), Periodic Narrowband Radio Wave Emissions and Inward Plasma Transport at Saturn's Magnetosphere, Ap J, 159, 249, 10.3847/1538-3881/ab818d, https://doi.org/10.3847/1538-3881/ab818d

Wyner, A. D. (1978), A definition of conditional mutual information for arbitrary ensembles, Info. and Control, 38, 51–59.

Xiang, Z., Tu, W., Li, X., Ni, B., Morley, S. K., & Baker, D. N. (2017). Understanding the

mechanisms of radiation belt dropouts observed by Van Allen Probes. *Journal of Geophysical Research: Space Physics*, 122, 9858– 9879. https://doi.org/10.1002/2017JA024487

Xiang, Z., Tu, W., Ni, B., Henderson, M. G., & Cao, X. (2018). A statistical survey of radiation belt dropouts observed by Van Allen Probes. Geophysical Research Letters, 45. https://doi.org/10.1029/2018GL078907

Zhao, H., Baker, D. N., Jaynes, A. N., Li, X., Elkington, S. R., Kanekal, S. G., Spence, H. E., Boyd, A. J., Huang, C.-L., and Forsyth, C. (2017), On the relation between radiation belt electrons and solar wind parameters/geomagnetic indices: Dependence on the first adiabatic invariant and L^*, *J. Geophys. Res. Space Physics*, 122, 1624– 1642, doi:10.1002/2016JA023658.

Zhao, H., Baker, D. N., Li, X., Jaynes, A. N., & Kanekal, S. G. (2018). The acceleration of ultrarelativistic electrons during a small to moderate storm of 21 April 2017. *Geophysical Research Letters*, 45, 5818– 5825. https://doi.org/10.1029/2018GL078582

rank	solar wind and magnetospheric parameters	i_{tr_max}	peak τ (hour)
1	V_{sw}	0.12	46
2	SYM-H	0.030	20–60
3	AL	0.020	50–80
4	P_{dyn}[a]	0.018	7–11
5	IMF |B|[a]	0.018	50–110
6	IMF $B_z < 0$[a]	0.017	50–110
7	n_{sw}[a]	0.016	7–11
8	IMF B_y[a]	0.012	0–16
9	Esw	0.012	40–90
10	IMF $B_z > 0$	0.011	0–16
11	σ(IMF B)	0.0083	0–10

Table 1. Ranking of the the solar wind and magnetospheric parameters based on information transfer to radiation belt electron PSD. Parameters 2–11 are calculated from CMI($x \rightarrow$ PSD$|V_{sw}$) where x = IMF |B|, $B_z < 0$, $B_z > 0$, B_y, Esw, and σ(IMF B). Parameter 1 from CMI($V_{sw} \rightarrow$ PSD$|n_{sw}$). i_{tr_max} = peak CMI – mean noise where noise is calculated for surrogate data (see Section 4.1).

[a] the response has dual mode: at small τ (τ < 15 hr) the response is electron loss and at large τ (τ > 40 hr) the response is electron enhancement. The ranking is based on the larger i_{tr_max} of the two responses (see text for explanation).

Parameters	Correlation	Peak τ (hr)	Conditional Mutual Information (CMI)	Peak τ (hr)
V_{sw}	**corr(V_{sw} → PSD)**	**38**	**CMI(V_{sw} → PSD| n_{sw})**	**46**
n_{sw}	**corr(n_{sw} → PSD)**	**15**	**CMI(n_{sw} → PSD| V_{sw})**	**7**
AL	**corr(AL → PSD)**	**53**	**CMI(AL → PSD| V_{sw})**	**76**
SYM-H	**corr(SYM-H → PSD)**	**40**	**CMI(SYM-H → PSD| V_{sw})**	**55**

Table 2. Highlighting the differences between correlation and CMI. τ = is the radiation belt response lag time.

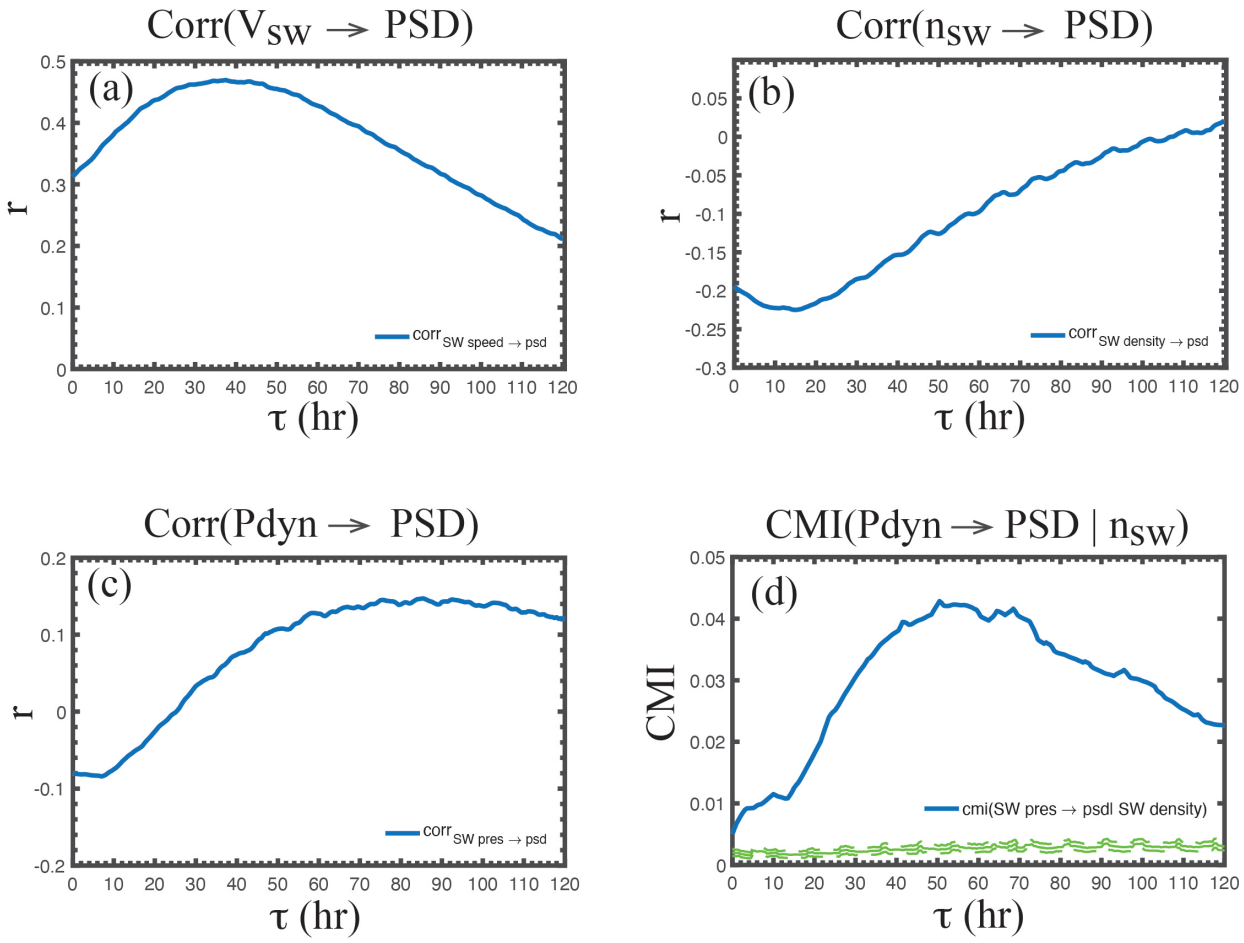

Figure 1. (a) V_{sw} positively correlates with radiation belt electron PSD. (b) n_{sw} negatively correlates with PSD. (c) The PSD response to solar wind dynamic pressure (P_{dyn}) has two modes: at small τ, P_{dyn} negatively correlates with PSD, similar to n_{sw} while at large τ, P_{dyn} positively correlates with PSD, similar to V_{sw}. (d) CMI(P_{dyn} → PSD| V_{sw}) is plotted as the blue curve. It shows that removing the effect of V_{sw}, the information transfer from P_{dyn} to PSD is similar to V_{sw} correlation with PSD, as expected. The mean noise and 3σ from the noise are plotted as solid and dashed green curves, respectively. The peak of the blue curve is 203σ above the mean noise and hence significant.

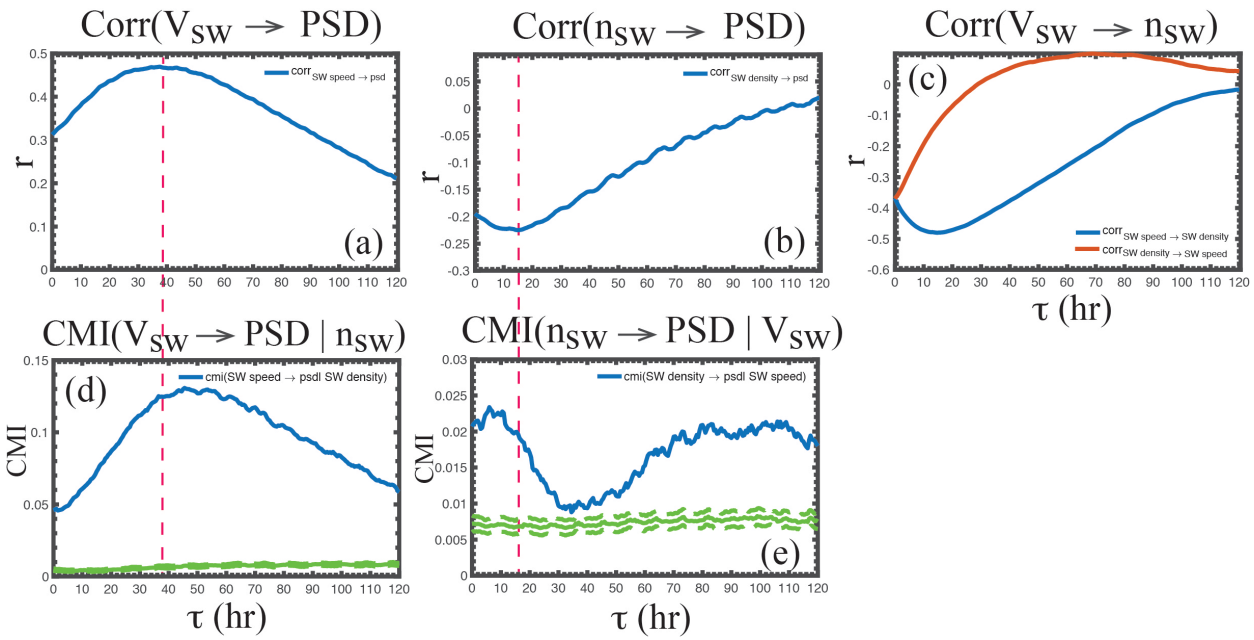

Figure 2. (a) V_{sw} positively correlates with PSD (same as Figure 1a). (b) n_{sw} negatively corelates with PSD (same as Figure 1b). (c) corr($V_{sw} \rightarrow n_{sw}$) = blue curve and corr($n_{sw} \rightarrow V_{sw}$) = red curve. The negative correlation between V_{sw} and n_{sw} raises the question that (a) or (b) may be coincidental. (d) CMI($V_{sw} \rightarrow$ PSD| n_{sw}) shows that (1) there is still information transfer from V_{sw} to PSD even after the effect of n_{sw} is removed and (2) removing the effect of n_{sw} shifts the peak of corr($V_{sw} \rightarrow$ PSD) to the right. (e) CMI($n_{sw} \rightarrow$ PSD| V_{sw}) shows that (1) there is still information transfer from n_{sw} to PSD even after the effect of V_{sw} is removed and (2) removing the effect of V_{sw} shifts the peak of corr($n_{sw} \rightarrow$ PSD) to the left. The red dashed vertical lines help visualize the shifts of the peaks in the correlations. CMI($n_{sw} \rightarrow$ PSD| V_{sw}) has a secondary peak at τ = 80–120 hr. The mean noise and 3σ from the noise are plotted as solid and dashed green curves, respectively.

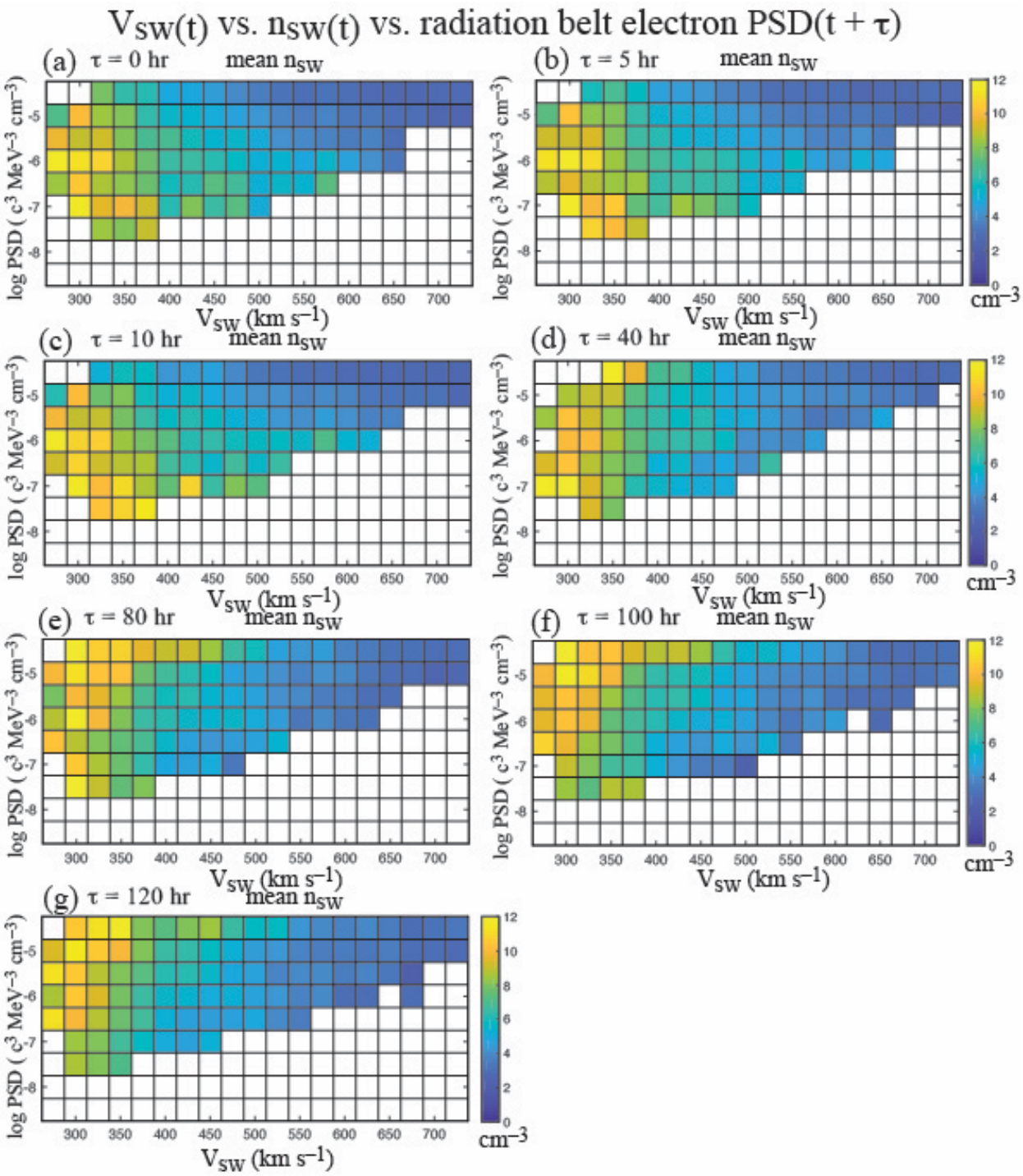

Figure 3. (a–g) log PSD(t + τ) vs. V_{sw}(t) vs. n_{sw}(t) for τ = 0, 5, 10, 40, 80, 100, and 120 hr, respectively. The color is n_{sw}. Large V_{sw} (V_{sw} > 450 km s^{-1}) corresponds to high PSD. For small V_{sw} (V_{sw} < 450 km s^{-1}), at small τ (τ = 0, 5, 10 hr), n_{sw} negatively correlates with PSD, but at large τ (τ = 80, 100, 120 hr), n_{sw} positively correlates with PSD. At τ = 40, the correlation is weak. Figure 3 is consistent with CMI(n_{sw} → PSD| V_{sw}) plotted in Figure 2e.

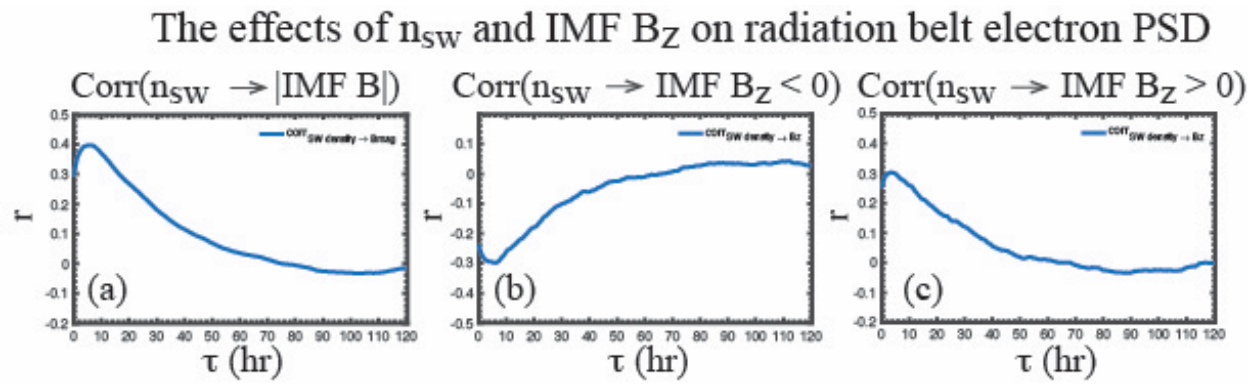

1168

1169 Figure 4. (a) n_{sw} positively correlates with |IMF B|. (b) n_{sw} negatively correlates with IMF $B_z < 0$.
1170 (c) n_{sw} positively correlates with IMF $B_z > 0$.
1171

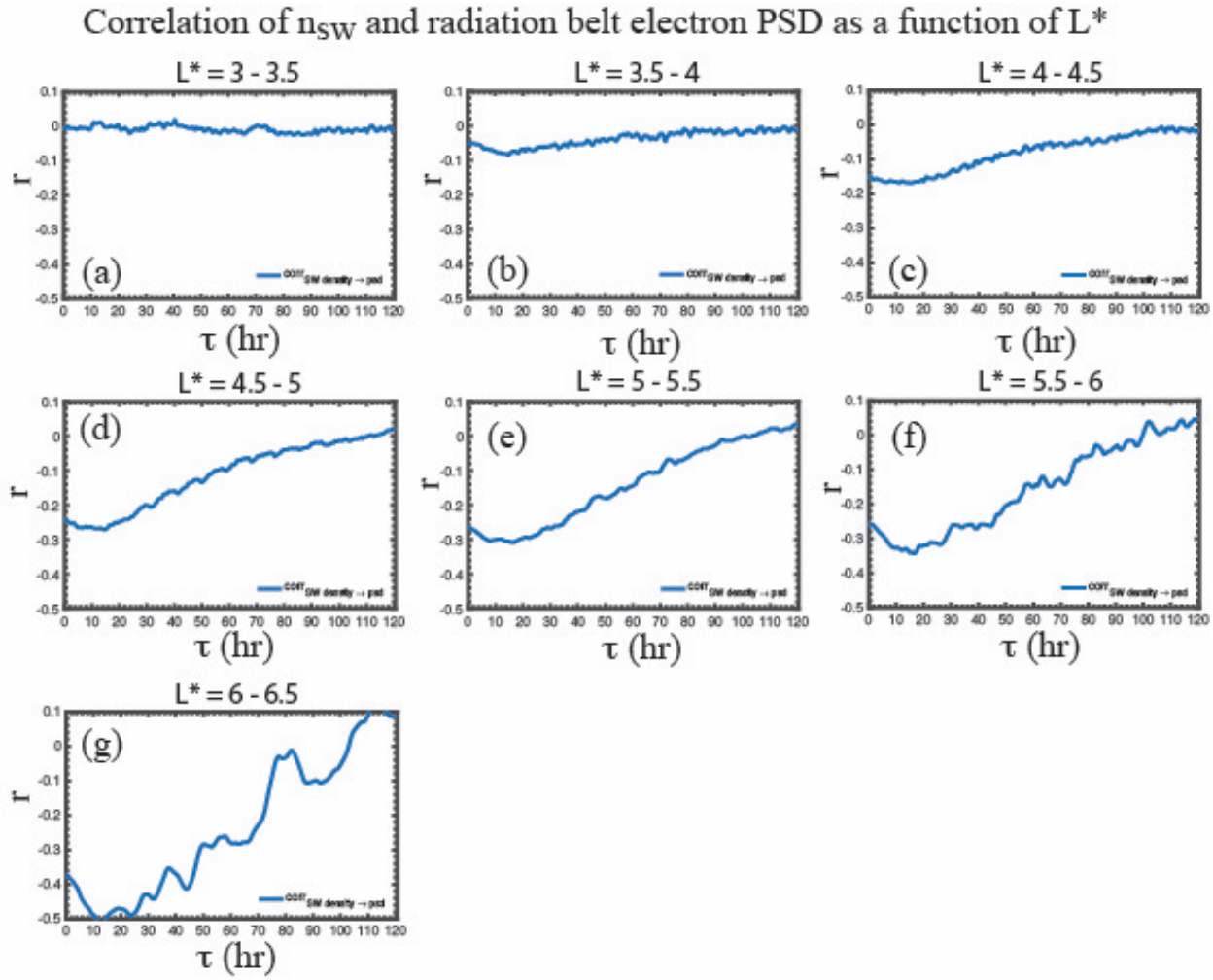

Figure 5. corr(n_{sw} → PSD) from L* = 3 to 6.5 in seven bins each with width = 0.5. (a) The correlation is insignificant at L* = 3–3.5, but slowly increases with increasing L*. (b–g) The correlations are significant ($p < 0.01$) at the minimum τ (τ = 15, 16, 17, 17, 17, 13 hr), r = (–0.086, –0.17, –0.27, –0.31, –0.34, –0.50), and n = (8,302, 11,481, 17,7891, 27,060, 6,236, 528), respectively.

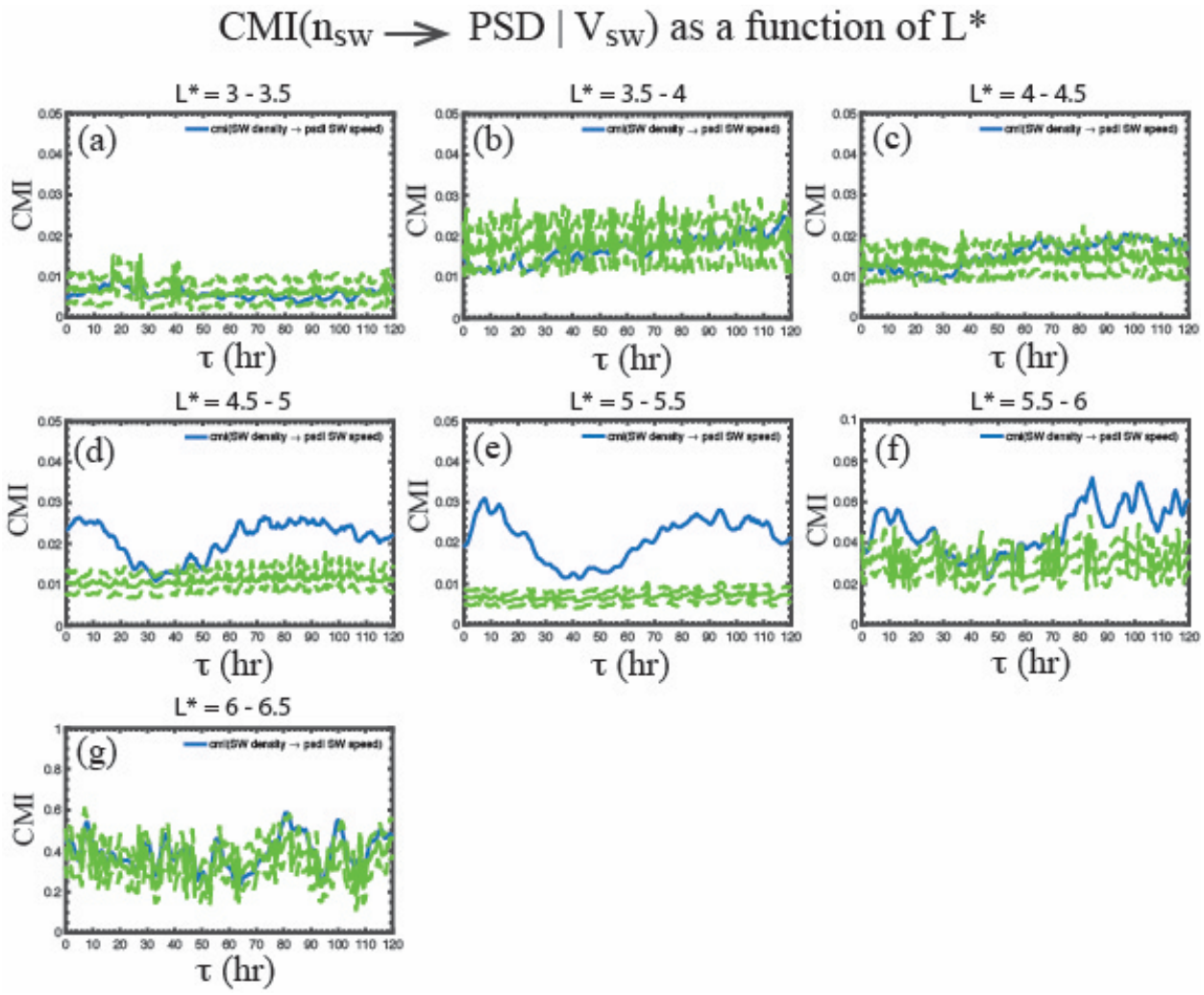

Figure 6. CMI($n_{sw} \rightarrow$ PSD| V_{sw}) from L* = 3 to 6.5 in seven bins each having width = 0.5. The mean noise and 3σ from the noise are plotted as solid and dashed green curves, respectively. (a) The CMI is at the noise level at L* = 3–3.5, which is consistent with the correlation in Figure 5a. (b–c) CMI is at the noise level at L* = 3.5–4.5, unlike the correlation in Figures 5a and 5b. (d–e) The peak CMI is significant at L* = 4.5–5.5 and (f) barely significant at L* = 5.5–6. (g) The CMI is at the noise level at L* = 6–6.5 where there is a large variability in PSD at this outermost L* layer.

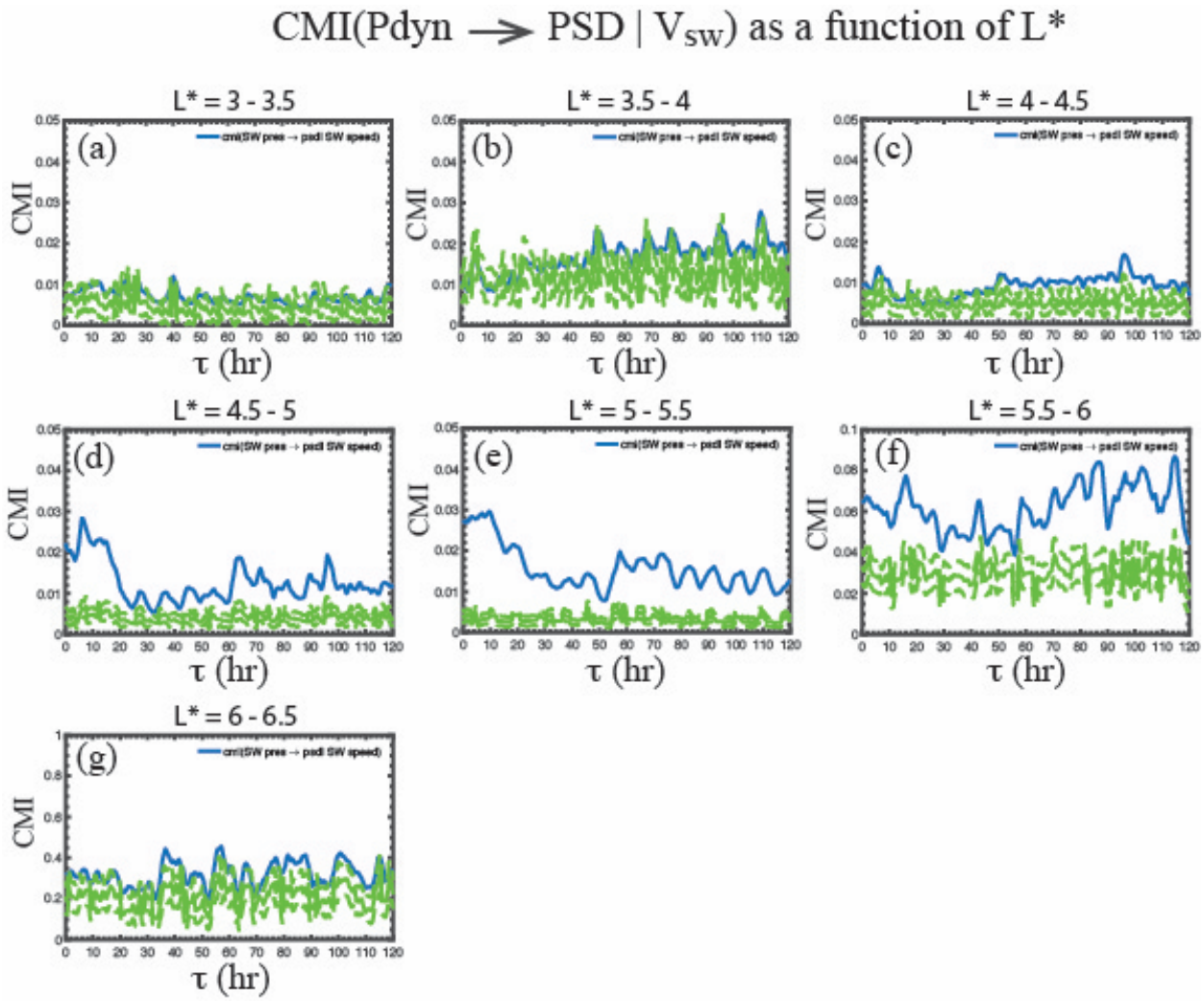

Figure 7. CMI(P_{dyn} → PSD| V_{sw}) from L* = 3 to 6.5 in seven bins in the same format as in Figure 6. The mean noise and 3σ from the noise are plotted as solid and dashed green curves, respectively. Similar to their counterparts in Figure 6 panels d–f, the primary peak CMIs are significant only at L* = 4.5–5.5 (d–e) and barely significant at L* = 5.5–6. The significances at L* = 4.5–6 are higher than their counterparts in Figures 6 panels d–f for CMI(n_{sw} → PSD| V_{sw}), suggesting that P_{dyn} is the real causal variable rather than n_{sw}. The opposite is true for the secondary peak, suggesting the causal variable is related more to n_{sw} rather than P_{dyn}.

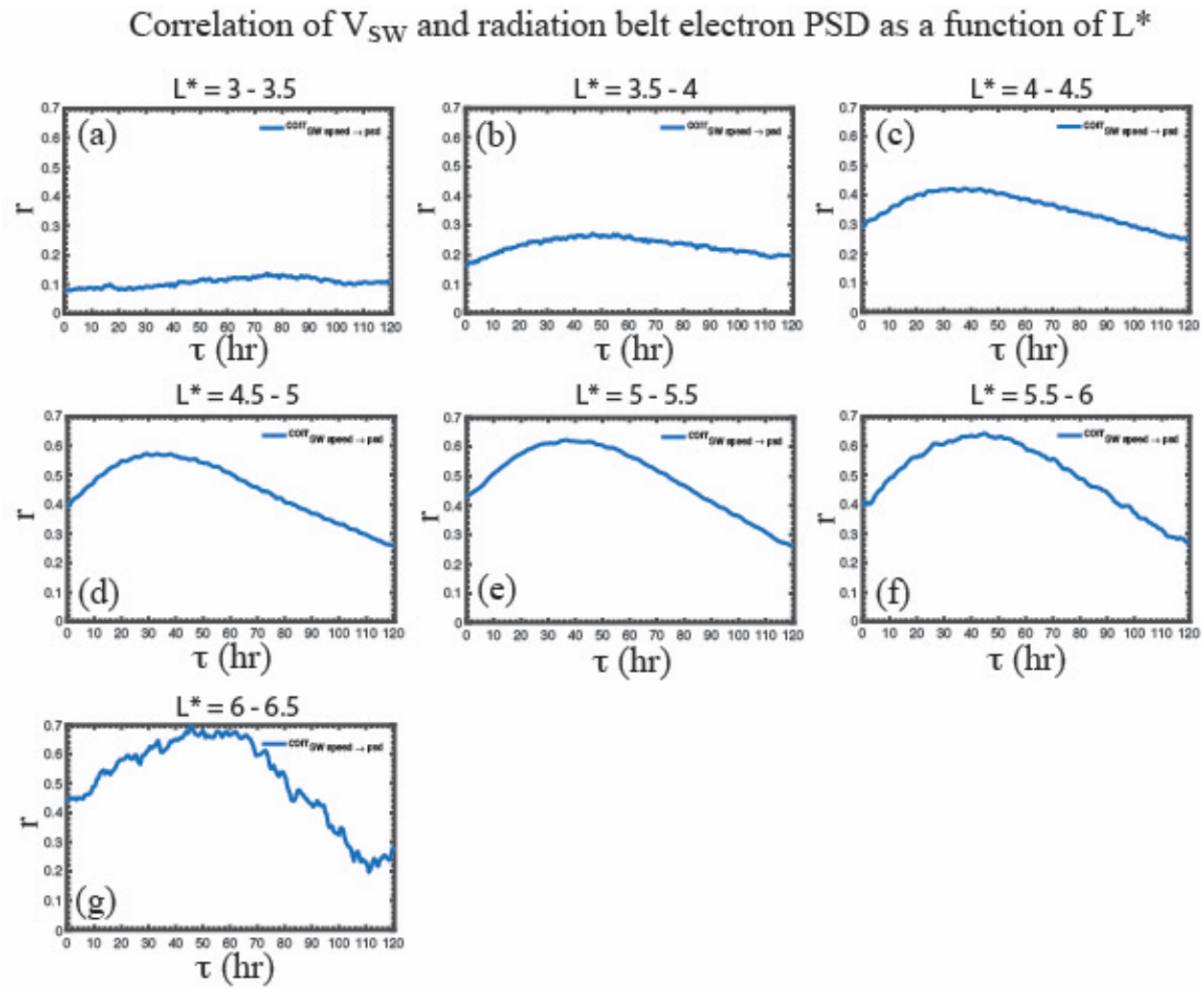

Figure 8. corr(V_{sw} → PSD) from L* = 3 to 6.5 in seven bins in the same format as Figrue 5. (a–g) The correlations are all significant at $p < 0.01$ at the maximum τ (τ = 40–120, 30–120, 38, 30, 37, 45, 30–90 hr), (r = 0.14, 0.27, 0.42. 0.57, 0.62, 0.64, 0.70) for L* = 3–3.5, 3.5–4, 4.–4.5, 4.5–5, 5–5.5, 5.5–6, and 6–6.5, respectively.

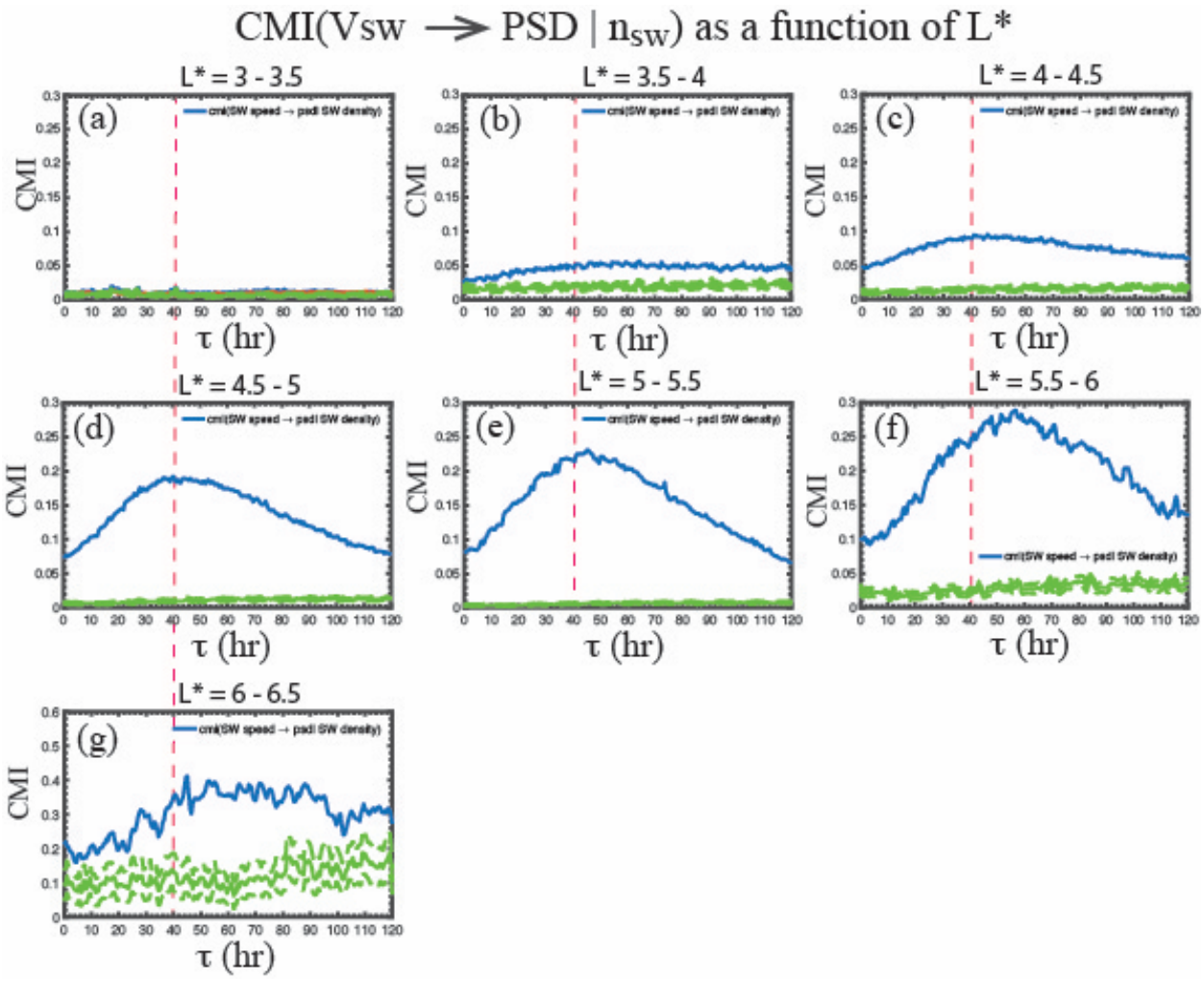

Figure 9. CMI(V_{sw} → PSD| n_{sw}) from L* = 3 to 6.5 in seven bins in the same format as Figure 6. The mean noise and 3σ from the noise are plotted as solid and dashed green curves, respectively. (a) The CMI is at the noise level at L* = 3–3.5, unlike the correlation in Figure 8a. (b–c) At L* = 3.5–4.5, the CMI has broad peaks from τ ~ 50 to 100 hr (or larger in the case L* = 3.5 – 4) and the peaks are significant. (d–f) At L* = 4.5–6, the CMI peaks are narrower (peak τ = 40, 46, 57 hr, respectively). (g) At τ = 6–6.5, the peak broadens again but remains significant.

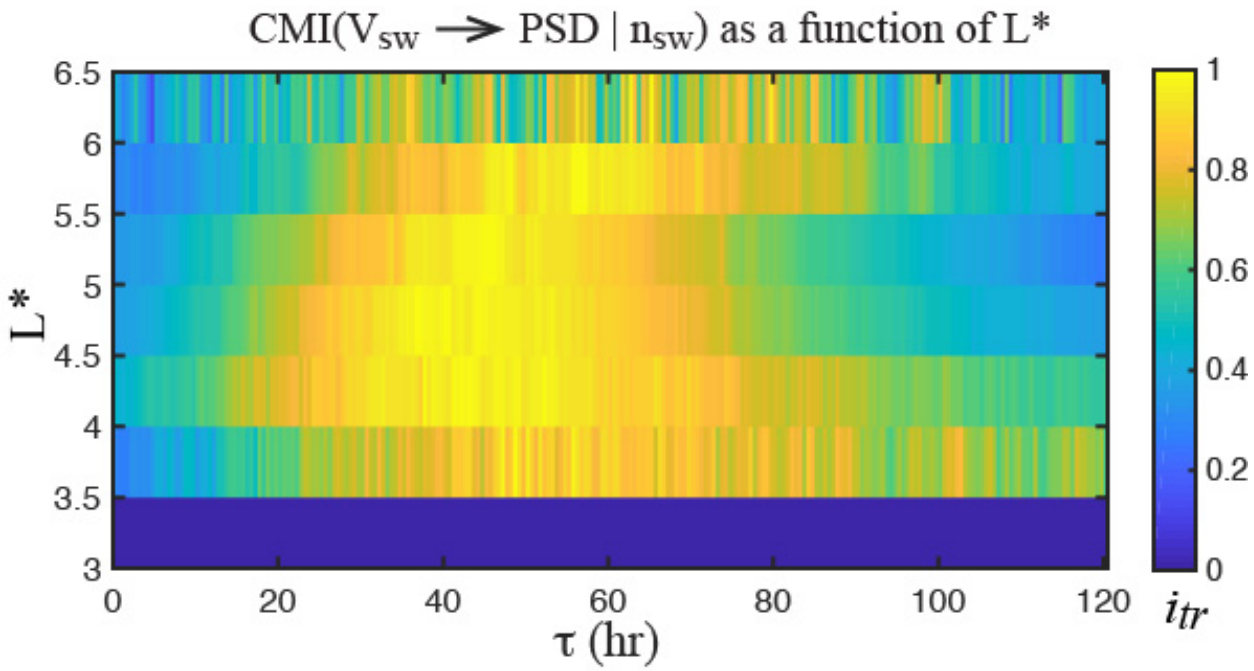

Figure 10. The normalized i_{tr} as a function of L* and τ where i_{tr} = the amount of information transferred = CMI($V_{sw} \rightarrow$ PSD| n_{sw}) – mean noise (the blue curve subtracted by the solid green curve in Figure 9). The orange and yellow correspond roughly to the top 20% of i_{tr} in each L* bin. The smallest peak τ can be found at L* = 4.5 –5.5 where τ = 35–50 hr. The peak τ broadens and shifts to larger τ at higher L* (t = 45–65 and 40–100 hr for L* = 5.5–6 and 6–6.5, respectively) and lower L* (τ = 35–55 and 45–60 hr for L* = 4–4.5 and 3.5–4, respectively). The broadening and shifting of the peak to higher τ may suggest outward and inward diffusion from L* = 4.5–5.5. At L* = 4–4.5, peak τ starts about the same time as that at L* = 4.5–5.5, which is suggestive of local acceleration at this L* band as well.

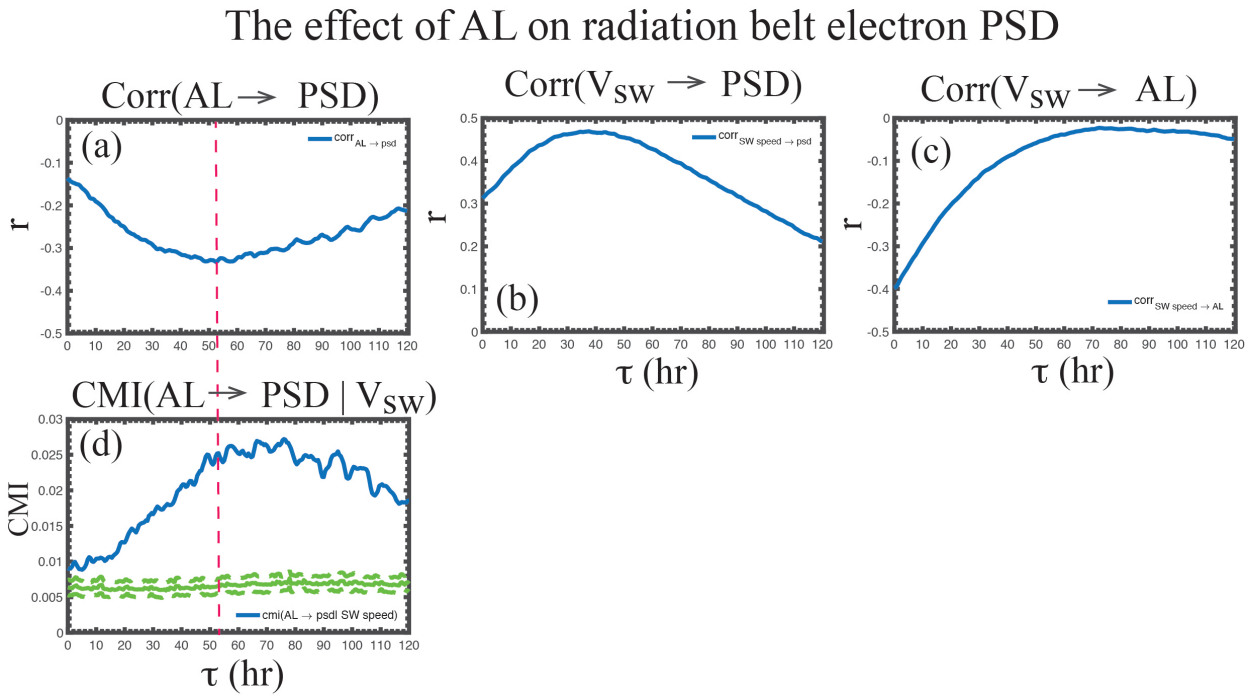

Figure 11. (a) AL negatively correlates with radiation belt electron PSD. (b) V_{sw} positively correlates with PSD (same as Figure 1a). (c) V_{sw} negatively corelates with AL. Given (b) and (c), the correlation in (a) may just be coincidental. (d) CMI(AL → PSD| V_{sw}) shows that even after the effect of V_{sw} has been removed, AL still has an effect on PSD. The mean noise and 3σ from the noise are plotted as solid and dashed green curves, respectively.

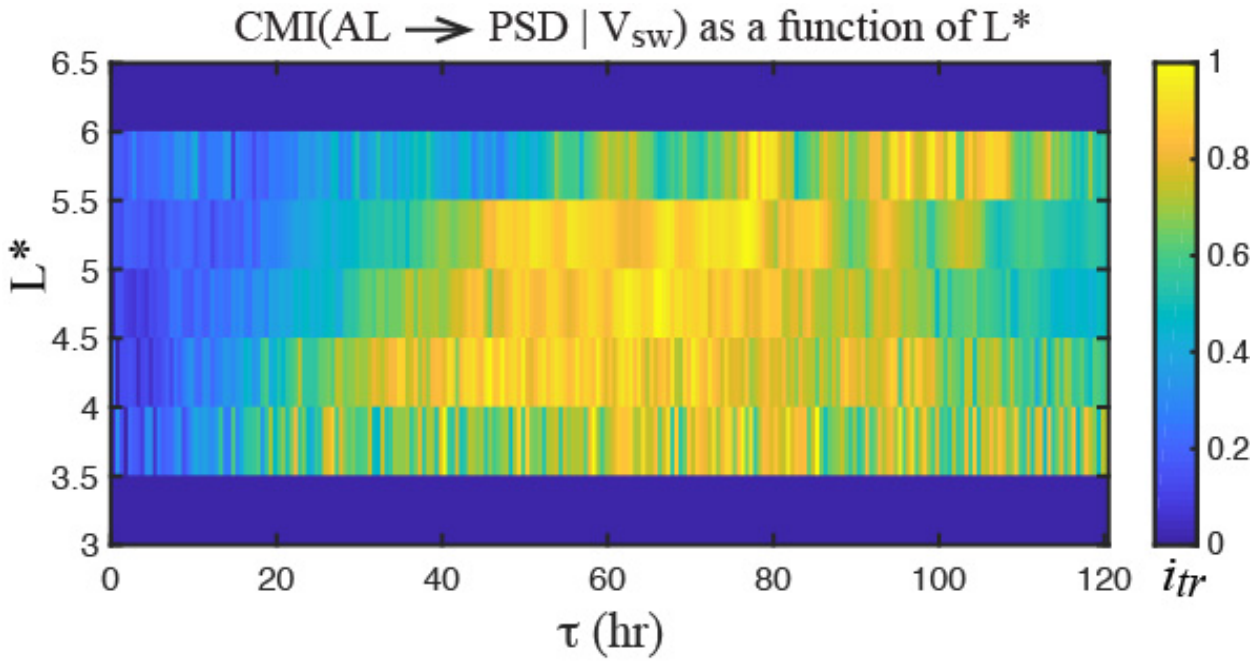

Figure 12. The normalized i_{tr} as a function of L* and τ where i_{tr} = the amount of information transferred = CMI(AL → PSD| V_{sw}) – mean noise in the same format as Figure 10. The orange and yellow correspond roughly to the top 20% of i_{tr} in each L* bin. The i_{tr} is at the noise level at L* = 3–4 and 6–6.5. The region with the largest significance is L* = 4.5–5 and 5 –5.5 with τ = 40–80 and 45–85 hr, respectively. The peak shifts to higher τ, τ = 75–100 hr, at L* = 5.5–6, suggesting outward diffusion from L* = 4.5–5.5. At L* = 4–4.5, the peak is the broad at τ = 35–80 hr. Because the peak τ starts about the same time as that at L* = 4.5–5, it may suggest local acceleration at this L*. The slow decay of τ suggests inward diffusion or longer lasting wave activity.

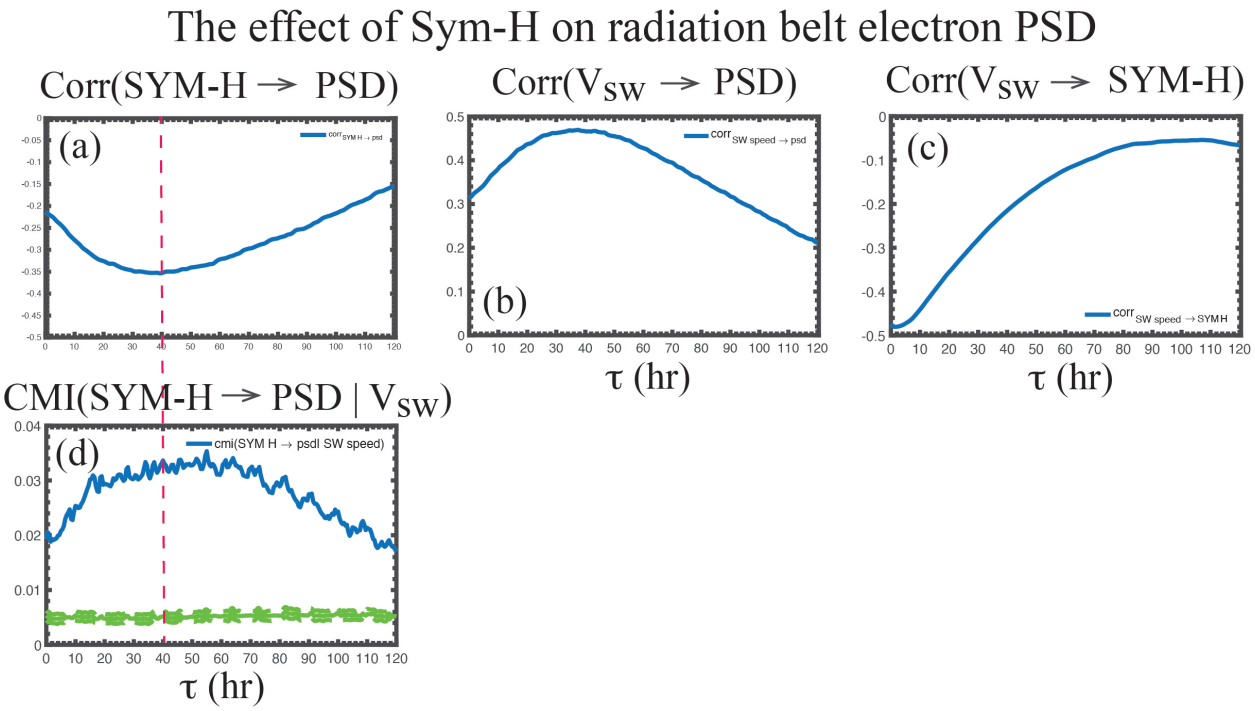

Figure 13. (a) SYM-H negatively correlates with radiation belt electron PSD. (b) V_{sw} positively correlates with PSD (same as Figure 1a). (c) V_{sw} negatively corelates with SYM-H. Given (b) and (c), the correlation in (a) may just be coincidental. (d) CMI(SYM-H → PSD| V_{sw}) shows that even after the effect of V_{sw} has been removed, SYM-H still has an effect on PSD. The mean noise and 3σ from the noise are plotted as solid and dashed green curves, respectively.

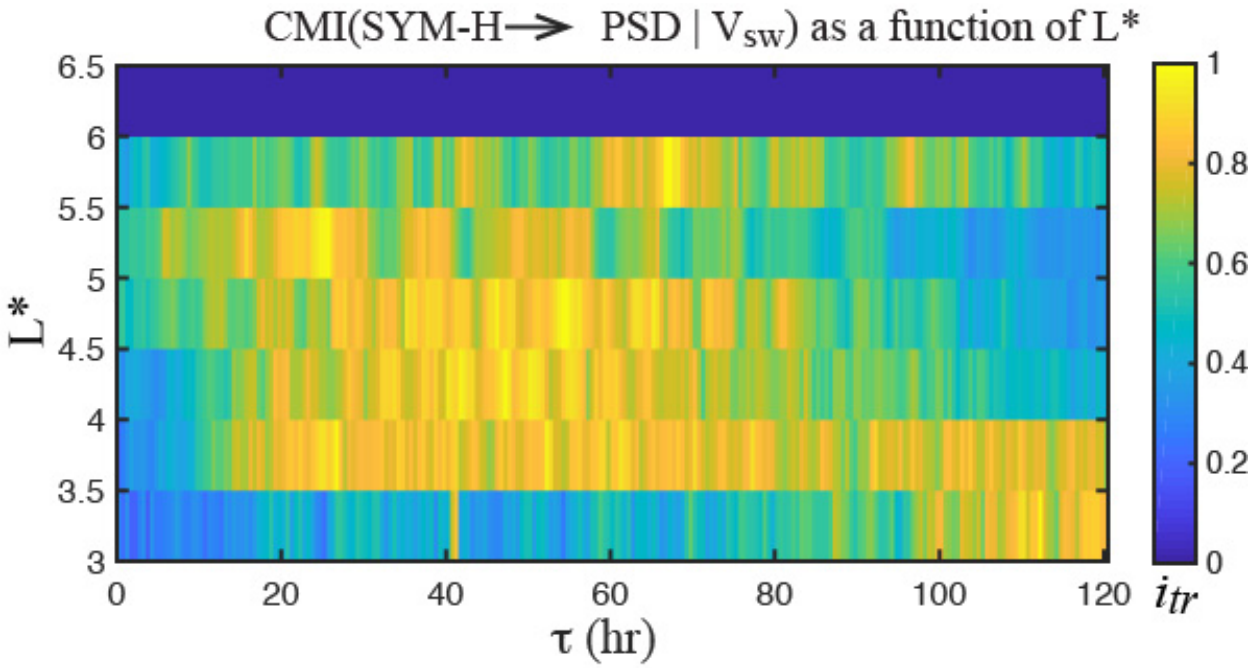

Figure 14. The normalized i_{tr} as a function of L* and τ where i_{tr} = the amount of information transferred = CMI(SYM-H → PSD| V_{sw}) – mean noise in the same format as Figure 10. The orange and yellow correspond roughly to the top 20% of i_{tr} in each L* bin. The i_{tr} is at the noise level at L* = 6–6.5 where there is a large variability in the radiation belt electron PSD. The highest peak significance can be found at L* = 5–5.5 with τ = 20–55 hr. The peak broadens and shifts to higher τ, τ = 60–75 hr at L* = 5.5–6, suggesting outward diffusion from L* = 5–5.5. At L* = 4–4.5 and 4.5–5, the i_{tr} peaks at τ = 30–60 and 30–75 hr. At L* = 3.5–4, the peak is very broad at τ = 20–120 hr, which may suggest local acceleration and inward diffusion from higher L*. At L* = 3–3.5, the i_{tr} peaks at τ = 110–120 hr or may be even higher, which may suggest slow diffusion from higher L*.